Chemical Engineering Journal Advances 5 (2021) 100070

Contents lists available at ScienceDirect

Chemical Engineering Journal Advances

journal homepage: www.elsevier.com/locate/ceja

A review on the development of visible light-responsive WO_3-based photocatalysts for environmental applications

J.C. Murillo-Sierra, A. Hernández-Ramírez*, L. Hinojosa-Reyes, J.L. Guzmán-Mar

Universidad Autónoma de Nuevo León, Facultad de Ciencias Químicas, Av. Universidad, Ciudad Universitaria, San Nicolás de los Garza, Nuevo León, Mexico

ARTICLE INFO

Keywords:
WO_3 based photocatalysts
Visible light
Environmental remediation
Water splitting
Photocatalytic conversion

ABSTRACT

The use of semiconductor photocatalysis is a promising, green, and sustainable technology to address solar energy conversion and environmental remediation issues. Among photocatalytically active semiconductors, considerable attention has been given to the visible-light active tungsten oxide (WO_3, Eg value ≈ 2.7–3.1 eV). This semiconductor has several advantages: strong absorption in the visible spectrum range, stability in acidic and oxidative conditions, low cost, and low toxicity. However, WO_3 presents fast recombination of charge carriers' and exhibits low photocatalytic activity for reduction reactions due to its conduction band potential (+0.5 V versus NHE). Many strategies have been applied to enhance photocatalytic activity and solar energy utilization of WO_3 by modifying the energy band position and reducing the charge carrier recombination. In this review, several approaches, such as designing with exposed facets and specific morphologies, doping with transition metals and non-metals, deposition of noble metals, and heterojunction construction, are summarized.

Moreover, the photocatalytic properties of the reviewed WO_3-based photocatalysts are discussed based on their environmental applications such as degradation of organic pollutants, air purification, CO_2 photoreduction, hydrogen production from water splitting and recently, simultaneous wastewater treatment and electric energy generation by photocatalytic fuel cells. Finally, the summary, future perspectives, and challenges of design novel WO_3-based photocatalysts with high efficiency are pointed out to meet the urgent demands of highly efficient technologies that use visible or solar energy for environmental applications.

Introduction

The continuous population growth and increasing global consumption of resources have triggered the shortage of nonrenewable resources. These energy-related activities have significant effects on the different environmental spheres (air, water, soil) [1]. Therefore, in recent decades, different strategies have been investigated to solve these issues. For example, solar energy conversion represents a promising strategy for several important applications, such as photocatalysis processes [1,2], photovoltaic cells [3], photothermal energy conversion [4], and photoelectrocatalysis [5,6]. Among them, heterogeneous photocatalysis is a technology used for pollutant degradation in water and air that has attracted the attention of many researchers since it represents an efficient alternative to clean the environment. This technology can directly utilize solar light to remove organic pollutants [7,8] and inorganic compounds [9] from water or volatile organic compounds (VOCs) [10] and polycyclic aromatic hydrocarbons (PAHs) [11] from indoor air. Moreover, photocatalytic reduction of CO_2 is a promising approach to convert this greenhouse gas into valuable compounds such as carbon monoxide (CO) [12], formic acid (HCOOH), formaldehyde (CH_2O) [13] and fuels such as hydrogen (H_2), methane (CH_4), methanol (CH_3OH) [14] and even C_1–C_2 compounds [15].

Heterogeneous photocatalysis is a well-described redox process that begins with light absorption by the semiconductor material. The following steps occur in the process: i) adsorption of reactants on the photocatalyst surface, ii) absorption of photons with equal or superior energy to the band gap, iii) transition of electrons from the valence band (VB) to the conduction band (CB), iv) transport of photogenerated electrons (e^-) and holes (h^+) towards the catalyst surface, v) redox reactions with adsorbed substrates, and finally vi) desorption of the products [16,17].

Titanium dioxide (TiO_2) has been the most widely studied catalyst for photocatalytic applications over the last few decades. Since the 1972 publication by Fujishima and Honda on the photoelectrolysis of water, TiO_2 has played an essential role in photocatalysis due to its low cost, chemical and photochemical corrosion stabilities, and nontoxicity [18]. Despite the advantages mentioned above, the photocatalytic process using TiO_2 shows significant drawbacks, such as the fast recombination rate of photogenerated e^-/h^+ pairs, low quantum yield in photocatalytic reactions in aqueous media, and wide band gap energy (E_g ≈3.2 eV), which limits its practical applications [7].

* Corresponding author.
E-mail address: aracely.hernandezrm@uanl.edu.mx (A. Hernández-Ramírez).

https://doi.org/10.1016/j.ceja.2020.100070
Received 30 September 2020; Received in revised form 9 December 2020; Accepted 15 December 2020

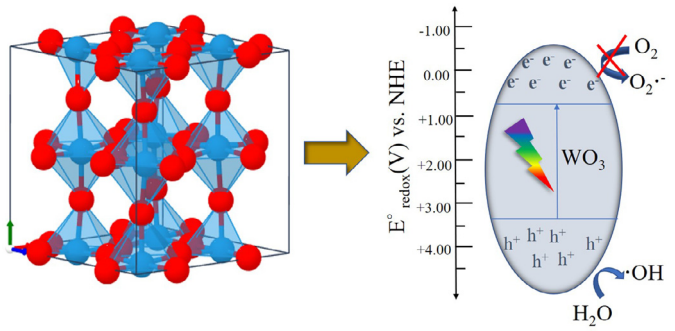

Fig. 1. Monoclinic tungsten oxide crystalline structure and the energy diagram.

Over the last four decades, different strategies have been studied to improve charge separation and extend TiO_2 activity into the visible light region, such as deposition or doping of noble metals or metal ions on its structure, coupled semiconductors and sensitization, which have generated promising results. However, alternative materials to TiO_2, which efficiently work under the visible light spectrum (E_g from 1.5 to 3.0 eV), are the trends for today's new photocatalysts in the field of environmental applications [19–22].

A suitable alternative is WO_3, which is a nontoxic, chemical, and photochemically stable semiconductor. In addition to its nontoxicity and stability in aqueous media over a wide range of pH values, the narrow E_g (2.7–2.8 eV) [19] is suitable for the absorption of visible light. Nonetheless, its high recombination rate of the photogenerated e^-/h^+ pairs limits its photocatalytic activity. Photocatalysis for environmental cleaning is perhaps the least developed application of WO_3 [23,24]. The WO_3 conduction band edge (ca. +0.5 V *vs.* NHE) is more positive than the reduction potential of O_2 ($O_2/O_2^{\bullet -}$= −0.33 V *vs.* NHE); thus, the photogenerated electrons in the CB of WO_3 could not reduce the adsorbed oxygen molecules via the single electron process to generate superoxide anion free radicals ($O_2^{\bullet -}$) [24]. Trapping of photogenerated electrons is necessary for the valence band holes to be available to oxidize organic molecules instead of being consumed in a recombination reaction.

On the other hand, the electronic properties, including the band gap, could be affected by the structure of WO_3. The WO_3 crystals are composed of corner and edge-sharing WO_6 octahedral units, and they have a rhenium oxide (ReO_3) cubic structure. Due to the thermal stability of WO_3, several distortions of the ideal cubic structure, such as monoclinic (γ-WO_3), triclinic (δ-WO_3), tetragonal (α-WO_3), and orthorhombic (β-WO_3) distortions, have been described. The monoclinic is the most stable phase of WO_3 (Fig. 1.) at room temperature (obtained between 17 and 330 °C), followed by the triclinic phase (–43 –17 °C). The orthorhombic WO_3 structure is produced by annealing at higher temperatures (330 –740 °C), and the tetragonal structure is obtained at temperatures >740 °C. α-WO_3 and β-WO_3 are stable phases at higher temperatures [25,26].

Different approaches have been proposed to further improve the photocatalytic performance of WO_3, i.e., morphological modifications [20,27–29], doping with metals, and nonmetals [30,31], and coupling with other semiconductors as the host or guest in heterojunctions [22,32]. In this review, the development of novel strategies to improve the performance of WO_3 is presented and discussed in depth. Different methods, such as foreign ion doping, noble metal deposition, and coupling with other semiconductors in heterostructures designed for efficient WO_3-based photocatalysts for environmental applications, have been reviewed. Although some reviews have been published related to WO_3 materials for different applications [26,33–36], this review is focused on WO_3-based photocatalysts that can be activated under visible or solar light and are a more sustainable alternative for developing new environmental technologies. The conclusions and perspectives for future research are addressed at the end of this article.

WO_3 facet design and morphological modifications

Several studies have suggested that morphology plays a significant role in the performance of photocatalysts [28,29,37–40]. Moreover, the specific surface area and optical band gap are strongly influenced by the crystalline phase, exposed facets, and shape of the nanostructures, all of which determine the photocatalytic activity [38]. In this context, WO_3 has been synthesized by different methods, such as anodization, sol-gel, spray pyrolysis, and hydrothermal methods, to obtain different morphologies with controlled characteristics, i.e., thin films [29,37], hierarchical nanostructures [39], shaped nanostructures [28,40,41], quantum dots (QDs) [42–44] and exposed facets [38,45].

In general, it is known that an optimum balance between high specific surface area and crystallinity is necessary to increase the photocatalytic performance [29,40]. For example, in the synthesis of thin films by spray pyrolysis, the surface area increased as the crystallite size decreased, and hence, the number of active sites on the photocatalyst surface was higher, increasing the degradation rate of organic compounds [37]. A higher annealing temperature, limited by the thermal stability of the catalyst, increases the crystallinity and can contribute to better performance. However, it is known that an increase in the annealing temperature produces a decrease in the surface area. Nevertheless, nanostructures with well-defined shapes can exhibit thermal stability, maintaining their properties, as reported by Mohamed *et al.* [29]. The authors found that nanoflakes of WO_3 are more stable with increasing temperature (Fig. 2a-d), while nanoporous structures collapse with increasing temperature, which decreases their surface area (Fig. 2e-h). Photoelectrochemical (PEC) experiments for water splitting revealed the highest photocurrent density response for nanoflakes as WO_3 photoanodes.

WO_3 quantum dots (QDs) combine different features, such as high specific surface area, extended light absorption ability, upstanding electron mobility and interesting effects, such as quantum confinement [43,46]. When WO_3 QDs are coupled to another photocatalyst, they have different functions to improve the photocatalytic activity. As reported by Liu *et al.* in 2018 [46], WO_3 QDs could improve the visible light absorption of graphene oxide-TiO_2 composites and thus enhance the spectral response. Furthermore, due to its quantum size, light conversion was higher in the composite with QDs than that of the composite without QDs, which was evidenced by the photocatalytic activity for RhB degradation. Another important feature is the specific surface area, which is greatly enhanced because of the high dispersion achieved with QDs. For instance, Chen *et al.* in 2019 [44] reported the coupling of WO_3 QDs on composite GO/TiO_2@SiO_2, demonstrating that after this modification, the specific surface area increased by almost 10%. This improvement was evidenced in the photocatalytic performance, where the composite with WO_3 QDs showed the highest degradation percentage for RhB solutions (98% within 60 min) under natural sunlight.

The morphology is not only related to the specific surface area but also closely related to adsorption-desorption during the catalytic process. The surface-active sites depend on the coordination number of the atoms, which is a function of nanostructure. For instance, atoms from the corners and edges in nanoplates or nanorods have more adsorption active sites than bulk atoms in nanospheres because of the low coordination number of the former. However, nanoplates exhibit the best photocatalytic activity on the degradation of RhB under visible light due to their cubic morphology (see Fig. 3) [28].

Otherwise, the surface atomic structure also strongly depends on the exposed facets in the photocatalyst surface [47]. The exposed facets (002), (020), and (200) in WO_3 are reported to have higher reactivity [38,39,45,47,48]. Xie *et al.* in 2012 [38] synthesized monoclinic WO_3 with facets exposed by a hydrothermal route under two different conditions. Quasicubic-like crystals were obtained using HF during the hydrolysis step, while sheet-like crystals were prepared using HNO_3 during the same step. The E_g and the energy level positions of the VB and CB

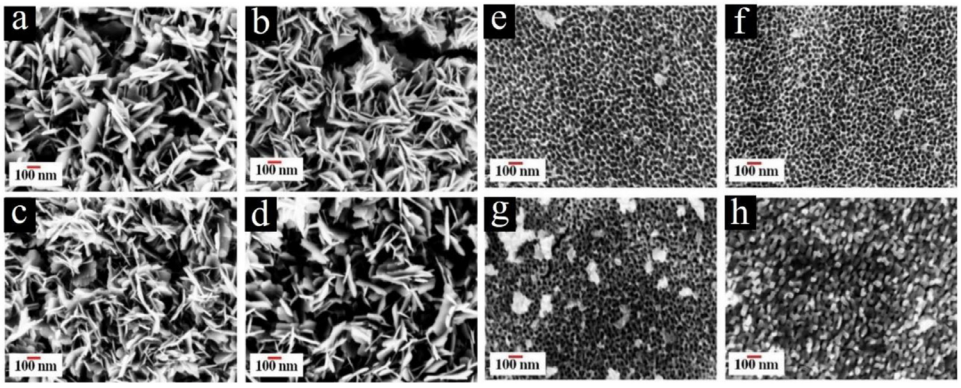

Fig. 2. FESEM images of nanoflakes WO_3 films in the air for 2 h (a) without annealing and annealed at (b) 300, (c) 400, and (d) 500 °C and nanoporous WO_3 films in the air for 2 h (e) without annealing and annealed at (f) 300, (g) 400, and (h) 500 °C (from [29]).

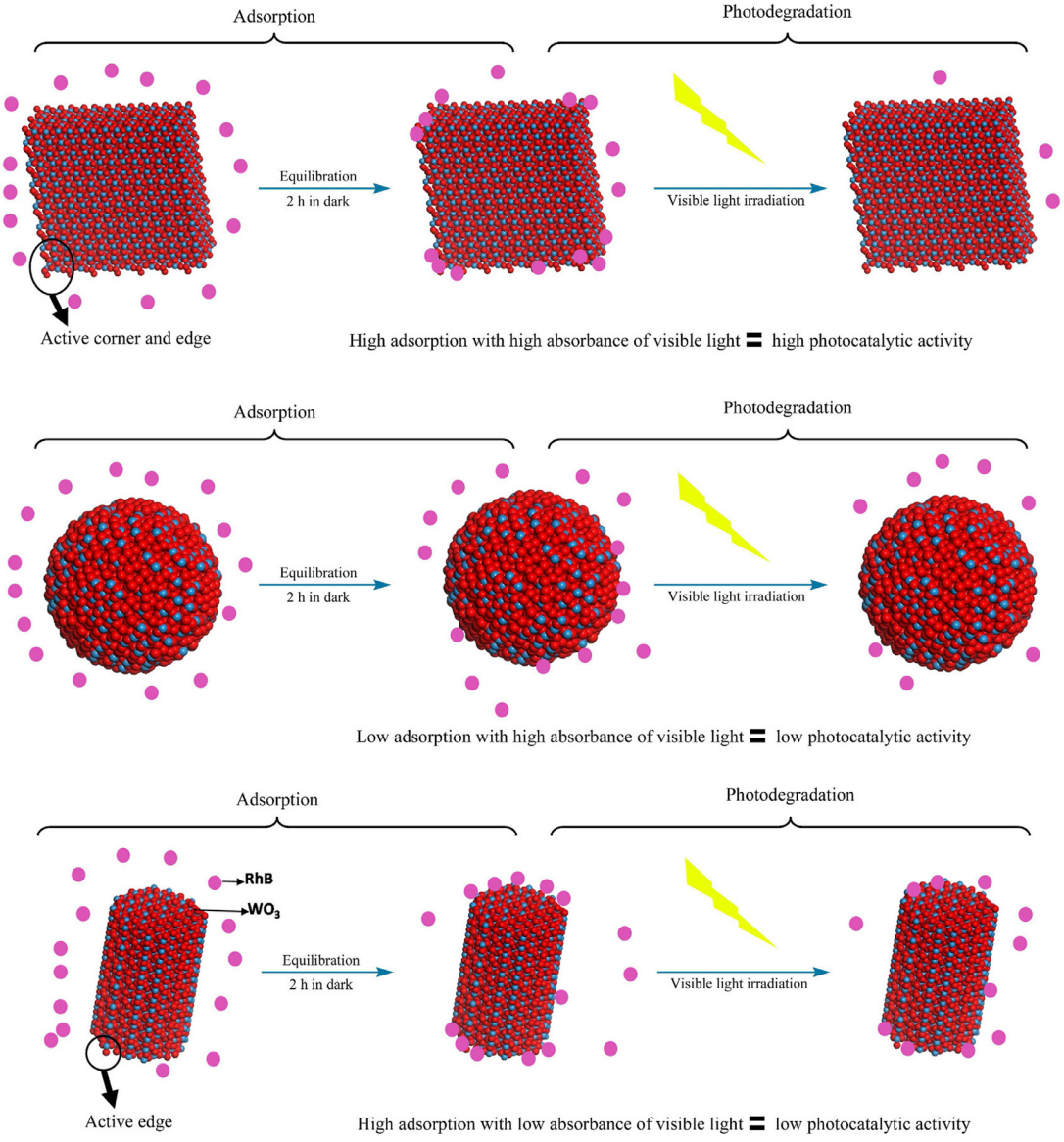

Fig. 3. Schematic illustrations of the shape effect on the photocatalytic activity of the WO_3 nanostructures (from [28]).

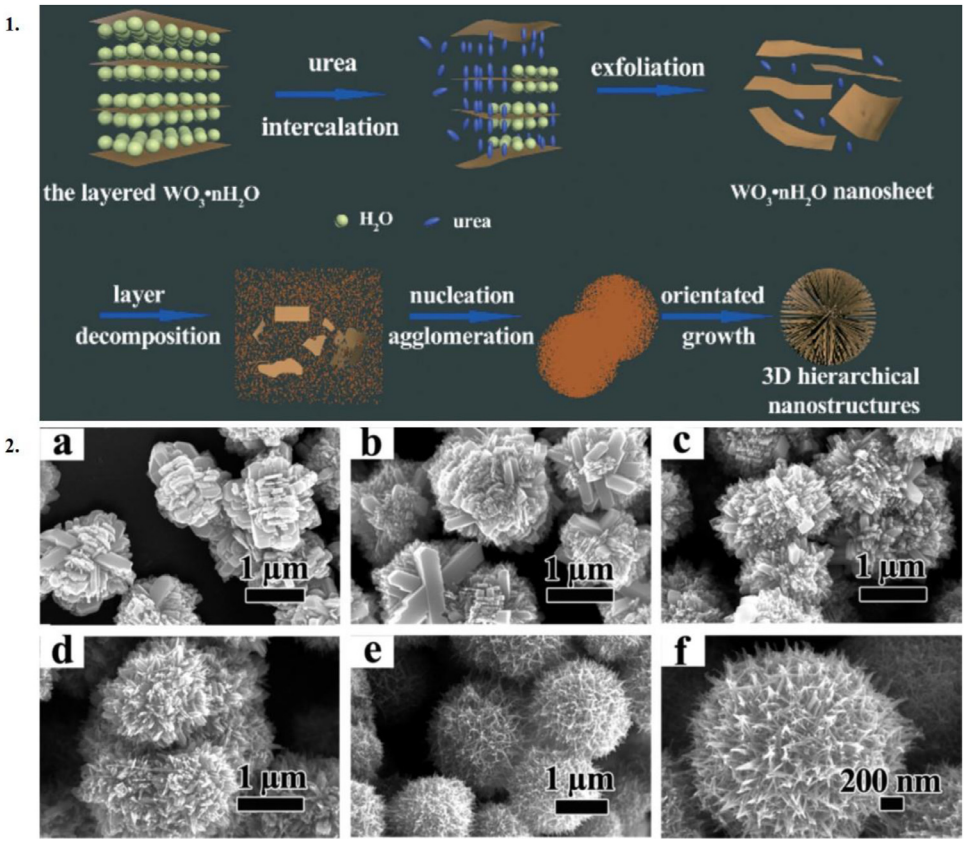

Fig. 4. 1. Schematic illustration of the formation mechanism of the hierarchical tungsten oxide nanostructures, and 2. SEM images of the as-prepared tungsten oxides with different amounts of urea: (a) 0.0 g (WU0); (b) 0.036 g (WU1); (c) 0.072 g (WU2); (d) 0.144 g (WU3); (e) 0.180 g (WU4) and its corresponding enlarged picture (f) (from [39]).

were influenced by the percentage of exposed facets in each nanostructure. For instance, sheet-like WO_3 crystals had a higher band gap energy (2.79 eV) than quasi-cubic-like WO_3 (2.71 eV). The sheet-like WO_3 crystals were mainly composed of (002) exposed facets in the top and (200) and (020) exposed facets in small amounts, and their CB energy level was 0.3 eV, which allowed CO_2 photoreduction to CH_4 (CH_4/CO_2 at −0.24 V).

As discussed previously, tuning of the exposed facets can modify the energy levels and band gap energy to enhance photoactivity. Different capping and directing agents, such as triethylamine [48], sodium sulfate (Na_2SO_4), ammonium sulfate ($(NH_4)_2SO_4$), and oxalic acid [45], have been used to obtain this preferential growth by hydrothermal synthesis. In this sense, Li *et al.* in 2015 reported that urea could be used as a directing agent to obtain faceted crystals with a hierarchical architecture formed by nanorods, nanobricks, or nanobelts with enhanced specific surface area (see Fig. 4) [39]. In 2017, the same research group demonstrated that in hierarchical nanostructures could simultaneously coexist with different crystal phases and different percentages of exposed facets. The crystal phases also have a close relationship with the exposed facets. Thus, (020) was a powerfully active facet for orthorhombic WO_3•$0.33H_2O$ but not for hexagonal WO_3. In hexagonal WO_3, the most active exposed facets were the (200) and (002) crystal planes, and their activity was assessed in the photocatalytic removal of rhodamine B (RhB), demonstrating that this facet tuning can improve the separation efficiency of the charge carriers, allowing complete removal of the dye in 100 min [47]. In Table 1, the most relevant results related to the performance of WO_3-based photocatalysts upon morphological modification are depicted.

Doping of tungsten oxide

Doping has been reported as a highly effective way to modify the adsorption edge of a semiconductor and improve its photoactivity under low-energy irradiation, which implies a redshift to the visible light region [50]. The principal effect of the inclusion of impurities in the doping process is to modify the position of energy levels or the inclusion of new ones, altering the electronic structure of the semiconductor. This modification benefits charge carrier separation, reducing the recombination rates, and this, in turn, could enhance the interface and surface characteristics [51–53]. In the case of WO_3, it has been demonstrated that doping with transition metals, noble metals, rare earth metals, and nonmetals could reduce the band gap or prevent the formation of e^-/h^+ pair recombination centers, thus improving the photocatalytic performance under visible light [54–57].

Transition metal ion doping

Transition metals are one of the most common impurities used for doping semiconductors due to their similar ionic radii. These ions can replace, e.g., W^{6+} in the WO_3 lattice, distorting the crystalline structure and narrowing the band gap [52,55,58,59]. Feng *et al.* synthesized Ti(IV)-doped WO_3 nanocuboids by a hydrothermal method. Ti^{4+} ions were incorporated into the lattice until reaching a 10% molar ratio, forming a finite solid solution; when this amount of Ti^{4+} was exceeded, a phase transformation occurred, and a tetragonal TiO_2 crystalline phase appeared [55]. In their experiments, they also proved that the Ti^{4+}-doped WO_3 photocatalyst with a 10% molar ratio was more active than 5% and 2% in the visible light region for RhB degradation (see Table 2). The addition of a titanium impurity forms energy levels between the VB and CB of WO_3, resulting in a reduced recombination rate due to the interaction with both VB and CB by either electron donation/acceptance.

Effective doping is more suitable for ions with similar ionic radii, as demonstrated by Song *et al.* in 2015. They prepared Fe-doped WO_3 nanostructures by a facile precipitation method using carbon spheres as a template with further calcination at 400 °C for 6 h. As the Fe content

Table 1
Relevant results of the facet design and morphological modifications of WO_3.

Photocatalyst	Synthesis method	Application	Experimental conditions	Results	Ref.
Quasi-cubic-like WO_3 and rectangular sheet-like WO_3 with a monoclinic crystal structure	Solvothermal	O_2 evolution and CH_4 production from CO_2 photoreduction	100 mg catalyst loading, 270 mL of $AgNO_3$ solution (3.15 g L^{-1}), 300 W Xe lamp (λ>400 nm) 50 mg of catalyst; diluted CO_2 (0.06 MPa), 300 W Xe lamp (λ>400 nm)	The quasi-cubic-like WO_3 exhibited high O_2 evolution. The sheet-like WO_3 was able to photo-reduce CO_2 yielding 0.34 μmol h^{-1} g^{-1} CH_4	[38]
Nanorods of hexagonal WO_3 with (200) exposed facet and nanosheets with (002) exposed facet	Hydrothermal	RhB degradation	40 mg catalyst loading, 40 mL of RhB solution (10 mg L^{-1}), 300 W Xe lamp (λ = 420 nm)	h-WO_3 nanosheets with (002) exposed facet showed 60% of RhB degradation in 80 min	[45]
WO_3 with different hierarchical structures	Hydrothermal	RhB degradation	20 mg photocatalyst loading, 40 mL of RhB solution (15 mg L^{-1}), 300 W Xe lamp (λ>400 nm)	o-WO_3.0.33$H_2$0 with (020) exposed facet showed 75% of RhB degradation in 80 min	[39]
Nanospheres, nanoplates, and nanorods with monoclinic phase	Hydrothermal	RhB degradation	0.1 g of photocatalyst, 100 mL of RhB solution (20 mg L^{-1}). 570 W Xe lamp (λ 400–800 nm)	75% of RhB degradation in 80 min, using nanoplate shape	[28]
WO_3 films with nano-porous or nanoflakes	Anodization	PEC H_2 production	A standard three-electrode cell in 1 M H_2SO_4. A SCE, and Pt foil as a reference and counter electrodes, respectively. 300 W Xe lamp (λ= 300 – 1100)	Nano-porous films achieved an IPCE of 9% and nanoflakes only ~ 2.5%	[29]
WO_3 thin films with rough surface morphology	Chemical spray pyrolysis	MO degradation	Photo-electrocatalytic degradation of MO (1 mM). WO_3 photoanode and a stainless-steel disk as a counter electrode. Tungsten filament lamp (λ=340 – 850)	98% of MO degradation after 360 min, confirmed by TOC and COD measurements	[37]
GO/WO_3 QDs/TiO_2 film	Hydrothermal	RhB degradation	0.2 g photocatalyst loading, 300 mL RhB solution (6×10^{-4} M), natural sunlight and a high-pressure Hg lamp (λ= 248 – 1014 nm)	98.18% of RhB degradation after 5 h, using GO/WO_3 QDs/TiO_2	[49]

increased from 0 to 8 mol%, no additional phases were detected in the Fe-doped WO_3 by XRD analysis [60]. The Fe^{3+} ions enter the WO_3 crystal lattice since the ionic radius of Fe^{3+} (0.64 Å) is similar to that of W^{6+} (0.62 Å). According to the UV–vis spectroscopy results, the Fe^{3+}ions create an impurity level above the valence band and thus narrow the band gap and improve the degradation of organic dyes such as methyl red and RhB under visible irradiation (420 nm) [31,60].

Moreover, when WO_3 was doped with transition metals with different ionic radii, such as Co^{2+} and Nb^{5+}, a similar behavior was observed [24,31,52]. For both ions, the crystal lattice of WO_3 was significantly distorted because of the dopant ion inclusion. This distortion induced more defects in the crystal lattice, such as oxygen vacancies, which promoted the production of reactive species on the catalyst surface and enhanced photocatalytic activity [24].

Noble metal doping and deposition

In general, the doping of metal-oxide semiconductors with noble metals is an effective way to promote the acceleration of photoexcited electron transfer from metal oxides to substrates [17,61]. Noble metals act on the semiconductor surface as a reservoir of electrons trapping conduction band electrons that could be used in multielectron reactions, *e.g.*, O_2 or CO_2 reduction [62]. This enhancement has been ascribed to the plasmonic energy transfer process in the interface between the metal and semiconductor [56], which allows efficient visible-light utilization. The enhancement by the surface plasmon resonance (SPR) effect has been utilized in the photocatalytic decontamination of water and air and water disinfection [63–65].

Commonly exploited noble metal dopants for WO_3 include Ag, Au, and Pt [56,64–67]. Hameed *et al.* [68] reported an improved light absorption in the visible region with an increase from 0.1 until a maximum Ag^+ loading of 5 wt% compared with bare WO_3. This behavior is attributed to the way electron transitions occur at the catalyst. In pure WO_3, the significant transitions are the transfer of electrons from the oxygen 2p orbitals to 4f orbitals in the W^{6+}or W^{5+} states. Furthermore, with the presence of Ag^+ on the semiconductor surface, these transitions occur from the VB of the O 2p orbitals to the lower Ag 3d orbitals, enhancing photon absorption in the visible region. This effect was also evidenced in the photocatalytic degradation of highly recalcitrant atrazine (see Table 2), where the catalyst with 1 wt% Ag loading on 40% WO_3/SBA-15 reached 68% pollutant degradation in 18 min under visible light, which was superior to that obtained by the 40%WO_3/SBA-15 sample (37% degradation) [56].

Ding *et al.* in 2017 [66] observed similar results for the degradation of RhB and methyl orange (MO) dyes with Ag nanoparticles (NPs) loaded onto WO_3 nanorods with exposed {001} facets. The band gap value (Fig. 5a) and the recombination rate (Fig. 5b) decreased with increasing Ag NP loading from 3.0 to 4.5 wt%. This finding was attributed to the SPR effect on the WO_3 surface. Additionally, the authors concluded that a strong relationship exists between the size of the Ag NPs and exposed facets in the semiconductor that is related to electron transfer and charge carrier separation.

The deposition of Pt and Au nanoparticles on the WO_3 surface has been reported as an effective strategy to avoid the recombination process in photocatalysis [17,23,61,62,64,69]. Qamar *et al.* proposed in 2011 that the photoactivity of deposited Au-WO_3 was highly size-dependent; the larger the size was, the lower its photoactivity (Fig. 5(c-d)). Meanwhile, Pt-WO_3 showed the best photocatalytic performance in the removal of MO and 2,4-dichlorophenoxyacetic acid (2,4-D) due to its smaller particle size, which avoided the shadowing of WO_3 and enhanced the number of metal deposits, which is traduced in increased electron traps for photogenerated electrons [61]. Another reason for the improved photocatalytic performance of the Pt-WO_3 catalyst is the easy formation of a Schottky barrier between the semiconductor surface and metal surface. When both the noble metal and semiconductor are in intimate contact, forming an interface, a Schottky barrier could be formed

Table 2
Relevant results on photocatalytic applications using WO_3 doped with transition metals, noble metal, and rare earth.

Photocatalyst	Synthesis method	Application	Experimental conditions	Results	Ref.
Nb doped WO_3	Hydrothermal	MB degradation	50 mg photocatalyst loading, 100 mL of MB aqueous solution (10 mg L^{-1}), 300 W high-pressure Hg lamp (λ= 248 – 1014 nm)	The (Nb/W atomic ratio = 0.03) catalyst showed the best degradation percentage (85%) in 120 min	[24]
Bi doped WO_3	Hydrothermal	PEC water splitting	A standard three-electrode cell in 0.1 M Na_2SO_4. Doped and undoped WO_3 working electrodes, a saturated Ag/AgCl, and Pt sheet as a reference and counter electrodes. 1000 W Xe lamp (λ=300 - 1100)	4-fold increase in photocurrent response using 0.17% Bi doping	[59]
Al doped WO_3	Hydrothermal	PEC water splitting	A standard three-electrode cell in 0.5 M H_2SO_4 electrolyte was used. Doped WO_3 photoanode, a saturated Ag/AgCl, and Pt as a reference and counter electrodes. 500 W Xe lamp (λ >400 nm)	The 0.77 wt% Al-doped WO_3 sample exhibited the maximum photocurrent density of 1.14 mA cm^{-2} at 1.2 V *vs.* Ag/AgCl	[58]
Fe-doped WO_3	Hydrothermal	PEC water splitting	A standard three-electrode cell in 0.1 M Na_2SO_4, WO_3, and Fe-doped WO_3 working electrodes, Pt foil, and Ag/AgCl counter and reference electrodes. 500 W Xe lamp (λ=300 – 1100 nm)	Photocurrent of 0.88 mA cm^{-2} for 2% Fe-doped WO_3	[78]
WO_3 nanorods and Pd -WO_3	Hydrothermal	2,4-dichlorophenoxyacetic acid (2,4-D) degradation	80–400 mg of photocatalyst in 200 mL of 2,4-D aqueous solution (40 mg L^{-1}). 300 W Xe lamp (λ=420 nm)	100% photocatalytic degradation after 90 min using 0.15 wt% Pd-WO_3	[79]
Fe doped WO_3	Co-precipitation	Methyl red dye	2 mg of photocatalyist in 20 mL of methyl red aqueous solution (10 mg L^{-1}). A 500 W tungsten lamp (λ=350 - 2500 nm)	94% degradation of methyl red after 120 min with 8 wt% Fe-WO_3	[31]
Ti(IV) doped WO_3 nanocuboids	Hydrothermal	RhB degradation	0.15 g catalyst loading in 50 mL of RhB aqueous solution (0.05 mM). 300 W Xe lamp (λ>420 nm)	Complete degradation of RhB after 70 min using 10 wt% Ti(IV)-WO_3	[55]
Pt/WO_3	Precipitation - wet impregnation	NO oxidation	NO concentration between 20 and 100 ppm. 500 W Hg-arc lamp (λ<350 nm), 500 W Xe lamp (λ=300–1100 nm), and a 500 W Xe lamp with (λ>420 nm)	NO conversions of ~ 40% with the Pt-WO_3 catalyst and 90% with the Pt-WO_3-zeolite molecular sieves when Xe lamp (simulated sunlight) was used	[64]
Ag-AgCl doped WO_3 hollow sphere	Deposition–precipitation–photoreduction	4-chlorophenol (4-CP) degradation	50 mg of catalyst in 100 mL of 4-CP aqueous solution (10 mg L^{-1}). 125 W metal halide lamp ($\lambda \leq$ 420 nm)	Degradation rate of 4-CP over 30Ag-AgCl/WO_3 was 11.7 times faster than that in pure WO_3	[65]
Photocatalyst	Synthesis method	Application	Photocatalytic test	Results	Ref.
Au NP@WO_3 NRs	Hydrothermal	RhB degradation	The catalyst in RhB aqueous solution (5 mg L^{-1}). 350 W Xe lamp (λ=200 – 800 nm)	100% degradation of RhB solution with 0.5 wt% Au NP@WO_3 NRs in 120 min	[69]
Ag/AgCl doped WO_3	Hydrothermal	RhB degradation	0.1 g of the photocatalyst. 50 mL RhB solution (10 mg L^{-1}). Simulated solar light as an irradiation source	degradation rate almost 10 times higher using 0.3 mol% doped catalyst	[67]
Silver loaded in mesoporous WO_3	Hard template - ultrasound-assisted insertion	Acetaldehyde degradation	0.2 g of the photocatalyst in a gas volume of 600 mL. 500 W Xe lamp (λ>420 nm)	90% of acetaldehyde degradation using m-Ag/WO_3 in 60 min	[80]
Ag/WO_3–110 nanorods	Hydrothermal - *in situ* photoreduction deposition	MO and RhB degradation	100 mg of the photocatalyst. 100 mL aqueous solution of MO (10 mg L^{-1}) / RhB (10 mg L^{-1}). 300 W Xe lamp (λ>420 nm)	>90% degradation of MO and RhB using Ag/WO_3–110 4.5 wt% catalysts in 210 min	[66]
Ag-WO_3/SBA-15 composite	Hard template - wet impregnation	Atrazine degradation	25 mg of catalyst in 25 mL atrazine solution (20 mg L^{-1}). 450 W Xe arc lamp (λ>400 nm)	68% degradation of atrazine in 18 min using 1 wt% Ag loading on 40% WO_3/SBA-15	[56]
Gd@WO_3NRs	Hydrothermal	RhB degradation	5 mg of the photocatalyst, in 50 mL of RhB solution (20 mg L^{-1}), metal halide lamp (λ = 420 nm)	94% degradation of RhB using 5 wt% Gd@WO_3NRs in 100 min	[81]

depending on the difference between its Fermi energy levels. In this case, photogenerated electrons at WO_3 CB can be channeled through the interface to the Pt nanoparticles, improving the charge carrier separation and therefore the photocatalytic performance [17]. Pt/WO_3 has also been studied for the efficient conversion of NOx on diverse carriers (e.g., ceramics, zeolite molecular sieves, activated carbon, and alumina) and using different light sources. The results are condensed in Table 2.

Rare-earth metal doping

Most of the studies on metal doping are related to transition metals or noble metals, but rare-earth doping can also improve the photocatalytic performance of semiconductor materials by modifying their physicochemical and optical properties [54,70,71]. Lanthanides possess partially empty *f* orbitals that can behave as donors or acceptors of electrons and holes and induce a redshift in the optical absorption [70,72].

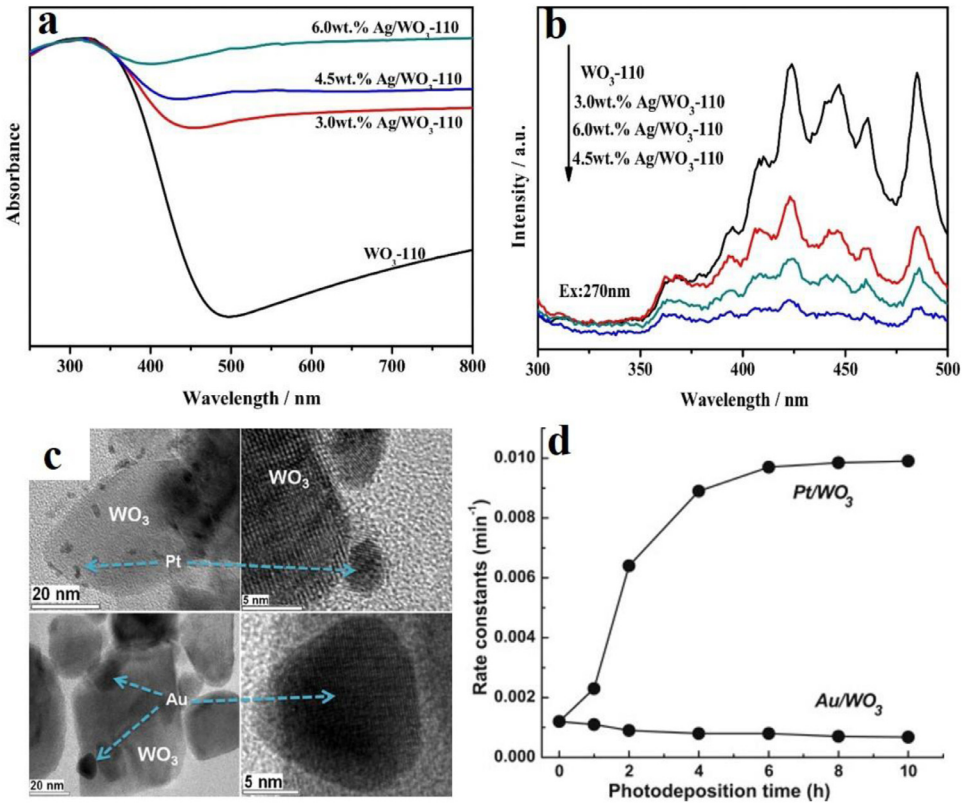

Fig. 5. a) UV–vis absorption spectra and b) photoluminescence spectra of WO_3 nanorods with different Ag loading amount (from [66]). c) Transmission and high-resolution transmission electronic micrography of WO_3 modified with Pt (1%) and Au (1%) nanoparticles and d) effect of photo-deposition time on the photocatalytic efficiency of nanocomposites (from [61]).

Additionally, an essential property of rare-earth doping is the formation of shallow energy levels between the VB and CB, improving the charge carrier separation [70,73]. Some of the most relevant examples of rare-earth WO_3 doping reported in the literature are europium (Eu^{3+}) [74], lanthanum (La^{3+}) [72], cerium (Ce^{3+}) [70], ytterbium (Yb^{2+}) [54], and dysprosium (Dy^{3+}) [75].

Regarding Eu^{3+} doping, Tahir *et al.* synthesized Eu-doped WO_3 by a hydrothermal route, obtaining assemblies with different morphologies and crystalline phases [74]. The Eu^{3+} incorporation percentage increases from 2 to 4 wt%, producing a decrease in the crystallite size, which improves the transfer of photogenerated charge carriers from the bulk to the surface of the catalyst. Moreover, the specific surface area increased from 29.89 m^2/g for bare WO_3 to 77.58 m^2/g for 4 wt% Eu-WO_3. These enhancements were evidenced in the photocatalytic tests, where methylene blue, RhB, and MO were completely degraded under visible light with the 4 wt% Eu-WO_3 photocatalyst. Similarly, Wang and Cao [71] prepared Eu^{3+}-doped WO_3 nanoparticles by a modified Pechini method for improved visible-light RhB photodegradation. The optical properties of the catalysts were evaluated, identifying a reduction of 17.2% in the forbidden band gap for Eu-doped WO_3 compared to bare WO_3, which was attributed to charge carrier transitions from Eu^{3+} *d* orbitals to W VB orbitals.

The formation of oxygen vacancy defects is another desirable effect described for rare-earth-doped WO_3, which has a significant influence on its photocatalytic activity [70,73,76,77]. The oxygen vacancies in the prepared catalysts could improve the efficient separation of photogenerated holes and electrons, increasing the surface reactivity due to the absorption of molecular O_2 and water that could lead to the formation of powerful radicals such as $O_2\bullet^-$ by a reduction reaction and •OH by oxidation. For instance, La^{3+}-doped WO_3 was successfully applied in the selective oxidation of CH_4 to CH_3OH under UVC-visible light, reaching a CH_3OH yield two times higher than that of bare WO_3, which was attributed to the formation of oxygen vacancies that increased the water absorption and modified the acid-basic properties in the catalyst [72].

Nonmetal doping

Nonmetal doping of WO_3 modifies the electronic structure of tungsten oxide. It may induce the formation of new energy levels within and above the valence band maximum (VBM) of WO_3, which can reduce the band gap, increasing its visible-light photoresponse and photocatalytic efficiency [51,82]. Another feature of nonmetal doping is its increased conductivity (photocurrent response), which is related to the efficient suppression of photogenerated e^-/h^+ pair recombination on the photocatalyst [83]. Some nonmetals, such as N, S, C, and F, have been successfully doped into WO_3 for photocatalytic applications. In Table 3, relevant applications of nonmetal-doped WO_3 are summarized. Among the nonmetal doping of WO_3, N doping has been highlighted as a promising method to improve WO_3 photocatalytic performance and visible light harvesting [30,82,84–86]. Nitrogen has an ionic radius similar to that of O atoms, and its lowest electronegativity can promote homogeneous doping by mixing its p states with O 2p states, yielding a reduction in the band gap [30]. In N-doped WO_3, the nitrogen atoms in the structure act as e^- traps preventing recombination with photogenerated h^+. These holes can interact with adsorbed species to produce hydroxyl radicals capable of oxidizing organic molecules such as amaranth on the surface [82].

Nonetheless, it has been reported that nitrogen incorporation also increases instability in the water splitting performance due to photocorrosion and excess lattice defects in the catalyst that create recombination centers. Hence, the extent of photogenerated carriers cannot be extracted during H^+/H_2 reduction, playing a negative role in the photocatalytic activity [57,84,87]. Doping with nonmetal molecules such as NH_4^+ [84] and N_2 [85] into WO_3 produced the same band gap reduction as described for N-doped WO_3 without the abovementioned drawbacks, with enhancement of the visible light absorption and photocurrent responses. Choi *et al.* reported that the NH_4^+ dopant works as an additional electron donor in the system, improving the conductivity and charge carrier transfer by increasing donor concentration [84].

Table 3
Relevant results on photocatalytic applications of non-metals doped WO_3.

Photocatalyst	Synthesis method	Application	Experimental conditions	Results	Ref
N-WO_3	Anodization and annealing in the presence of N_2 and NH_3/N_2 mixture	MO degradation	The concentration of MO was 20 mg L^{-1}. N-WO_3 as working electrode, Pt and Ag/AgCl (KCl saturated) as counter and reference electrodes. 500 W Xe lamp (λ> 400 nm).	N-doped showed a higher rate constant (0.0473 min^{-1}) than undoped one (0.0352 min^{-1})	[30]
S-WO_3	Solid-state annealing	Water splitting	A standard three-electrode cell in 0.5 M H_2SO_4, S-WO_3 working electrodes, Pt foil, and Ag/AgCl counter and reference electrodes. 500 W Xe lamp (λ>400 nm)	Increased photocurrent response from 0.67 to 0.82 mA cm^{-2} with 2.0 wt% S-WO_3	[57]
			3.57 g L^{-1} photocatalyst in 16 mM Fe^{3+}as an electron acceptor	Maximum of 99 μM g^{-1} h^{-1} H_2 with 2.0 wt% S-WO_3 material	
N-WO_3	Thermal decomposition with urea	Amaranth degradation	0.5–2 g L^{-1} of the photocatalyst in 100 mL of amaranth solution (5–25 mg L^{-1}). Metal halide lamp 160 W (λ>400 nm) and a 13 W blacklight lamp (λ>350 nm)	100% degradation with visible and UVA irradiation by using N-WO_3 catalyst	[82]
S-WO_3 nanowires	Hydrothermal	MO degradation	30 mg of the photocatalyst in 15 mL of 20 mg L^{-1} MO solution. A 300 W Xe lamp (λ>420 nm)	97% degradation in 180 min using 3 wt% S-WO_3	[83]
C-WO_3.0•33H_2O	Hydrothermal	RhB degradation	50 mg of the photocatalyst in 100 mL RhB solution (10 mg L^{-1}). 300 W Xe lamp (λ=300 – 1100 nm)	Enhanced degradation rate up to 2 times with 0.1% C-doped WO_3 allowing complete degradation of RhB in 180 min	[94]
I-P co-doped WO_3	Precipitation method	Amaranth degradation	1 g of the catalysts in 0.1 L of dyeing wastewater. Natural sunlight	93.4% TOC, 95.1% COD abatement using I-P co-doped WO_3	[93]
F-doped WO_3 plate-like films	Hydrothermal	MO degradation	MO solution (20 mg L^{-1}) in a quartz reactor. 300 W Xe lamp (λ> 400 nm)	High degradation rate of MO, 6×10^{-2} min^{-1} F-doped WO_3 plate-like film.	[91]
S:WO_3 and I:WO_3	Spray pyrolysis and ultrasonic spray nozzles	PEC water splitting	A standard three-electrode cell in 1 M methane sulfonic acid with 0.1 M methanol, S-WO_3 and I-WO_3 working electrodes, Pt wire, and Ag/AgCl counter and reference electrodes. 150 W Xe lamp (λ=300–1100 nm)	The 0.1% S doped WO_3 exhibited improved full-spectrum and visible light photocurrent response compared to undoped WO_3 and 0.1% I:WO_3	[88]
xN_2•WO_3	Manually sprayed using an airbrush	PEC water splitting	A standard three-electrode cell in 1.0 M HCl, xN_2-WO_3 working electrodes, Pt mesh, and Ag/AgCl counter and reference electrodes. 150 W Xe lamp (λ=300–1100 nm).	The maximum amount of O_2 produced using a 0.039N_2•WO_3 electrode was 80 ± 3 μg	[85]
C doped WO_3 films	Spray-pyrolysis deposition	PEC water splitting	A standard three-electrode cell in 1.0 M HCl, C-WO_3 working electrodes, Pt foil, and Ag/AgCl counter and reference electrodes. 150 W Xe lamp (λ=300–1100 nm).	Photocurrent of 1.6 mA cm^{-2} using 1 M HCl electrolyte and 2.6 mA cm^{-2} using methanol as a sacrificial agent using C-doped WO_3	[89]
F-doped WO_3 (~0.25at%)	Solid-state sintering	PEC Water splitting	3.57 g L^{-1} photocatalyst in 16 mM Fe^{3+}as an electron acceptor. A 250 W high-pressure Hg lamp, (λ=300–400 nm)	F-doped WO_3 showed higher oxygen production rate (102.1 µmol•L^{-1}•g^{-1}•h^{-1}) under UV irradiation, compared to that of WO_3 (80.2 µmol•L^{-1}•g^{-1}•h^{-1})	[92]
NH_4-doped anodic WO_3	Anodization and subsequent NH_4OH treatment by a wet-based	Water splitting	A standard three-electrode cell in 0.33 M H_3PO_4, NH_4-WO_3 working electrode, Pt mesh, and Ag/AgCl counter and reference electrodes. 300 W Xe lamp (λ=300–1100 nm	The doping of NH_4^+ generated the $(NH_4)_{10}W_{12}O_{41}$ phase during the NH_4OH treatment, leading the E_g reduction from 2.9 to 2.2 eV, enhancing the water splitting performance	[84]

Another alternative nonmetal dopant reported in the literature for modifying WO_3 is S doping [83,88]. S doping has been demonstrated to be an effective method to reduce the E_g and increase the photocurrent response, which means better performance in photocatalytic reactions. Since the ionic radius of the S^{2-} anion (1.7 Å) is significantly higher than that of O^{2-} (1.22 Å), doping by anion substitution to generate the W-O-S bond is difficult. Then, the most favorable mechanism is cation substitution due to the similar ionic radius between W^{6+} (0.6 Å) and S^{6+} (0.29 Å), forming W-S bonds [57]. Han *et al.* reported in 2016 a reduction in the E_g from 2.62 eV for pure WO_3 to 2.52 eV for 1–4 wt% S-doped WO_3. The 3 wt% S-doped WO_3 showed a considerable enhancement in the visible light-responsive photocatalytic degradation of MO, allowing 97% removal in 180 min [83].

Similarly, WO_3 doped with carbon has shown improved photocatalytic activity in the visible region because this nonmetal can also boost the light absorption range to longer wavelengths. The carbon doping samples were obtained by using glucose as a carbon source through spray-pyrolysis deposition [89] or adding the carbon dopant via a mild liquid phase method [90] (a carbonized product of glucose obtained by the hydrothermal method was treated with HNO_3). However, these calcination procedures as spray pyrolysis methods yield a low carbon doping level compared to the doping concentration added [90]. The slight reduction in the cell parameters due to interstitial carbon doping induced WO_6 octahedral distortion. In addition, carbon doping also induces the formation of new energy levels above the valence band. The new level increased the visible absorption edge of WO_3 and the migra-

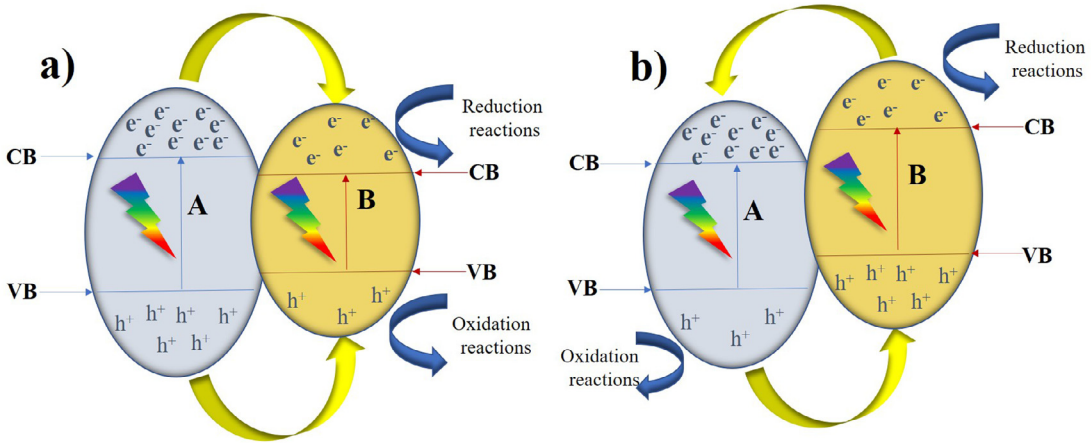

Scheme 1. Illustration of the charge carriers' transfer mechanism in a) type I and b) type-II heterojunctions.

tion pathway of photogenerated carriers, which reduced the carriers' recombination rate [90].

Doping WO_3 with fluorine has been carried out by fluoride incorporation using HF by the hydrothermal method [91] and NH_4F by the low-temperature solid-state sintering method [92]. Jin and Liu described that although F^- doping did not cause significant redshifting in the fundamental absorption edge of WO_3, F^- incorporation caused the enhanced absorption of visible light, showing the highest photocatalytic activity for water splitting under both UV and visible light attributable to the increased number of oxygen vacancies in the catalyst. The enhanced surface oxygen vacancy concentration was demonstrated by the resistivity reduction of the catalyst, increased adsorbed oxygen, and the generation of W^{5+} for charge compensation of the catalyst surface [92].

In addition to single nonmetal doping, nonmetal codoping (P/I) was reported in the literature for WO_3, allowing enhanced specific surface area and low E_g value. The substitutional and interstitial occupation of oxygen vacancies (O^{2-}) into the WO_3 framework by I^- and P^{3+} ions formed I-P-$WO_{(3-x)}$. The enhancement in the photocatalytic performance of P/I-codoped WO_3 was demonstrated under simulated solar light compared to pure or single P- and I-doped WO_3 [93].

Semiconductor coupling

Semiconductor coupling is a promising strategy to develop efficient photocatalytic materials exhibiting synergistic effects attributed to the enhancement of the light absorption capability, an increase in the active sites for reactions, and a significant reduction in the recombination rate of e^-/h^+ pairs [95]. This coupling can be a simple catalyst mixture in solution [96] or an efficient heterojunction [97–99], in which the charges strongly interact between the semiconductors and reactants. In this context, WO_3 has been investigated in various types of couplings, with type II and Z-scheme heterojunctions being the most effective.

Type II heterojunction

A heterojunction is the combination of two or more nanostructured materials that present an atomic-level in-plane adjustment. The formation of a heterojunction by combining WO_3 with another semiconductor having unequal band edge positions can provide band alignment to enhance the separation efficiency of photoinduced charges and the photocatalytic performance. Three types of conventional heterojunctions have been described depending on the transfer mechanism of the charge carriers in the photocatalysts (type I, II, and p-n) [100]. In heterojunction type I, both the CB and VB positions of semiconductor B are placed between those of semiconductor A (Scheme 1a), for which electrons and holes are transferred to compound B. This movement allows better separation; however, since the charge carriers accumulate in semiconductor B with a narrow band gap, the recombination rate is increased, and the photocatalytic efficiency is lower. Conversely, in heterojunction type II, which is most preferred for photocatalytic applications, the positions of the CB and the VB levels of semiconductor A are higher than those of semiconductor B (Scheme 1b). The difference in chemical potential between semiconductors A and B causes band bending at the interface junction. Thus, the migration of photogenerated electrons and holes in the opposite direction could be promoted under light irradiation, resulting in the spatial separation of e^-/h^+ pairs [100,101]. Moreover, the synergistic interaction between different semiconductor phases strongly depends on the synthesis method and physical properties of the resulting materials (particle size and shape, specific surface area, crystallinity, electronic structure, among others). [102]).

WO_3/TiO_2 and WO_3/ZnO heterostructures have been evaluated in photocatalytic applications since the coupling of a low band gap material (WO_3) with TiO_2 and ZnO forms a type II heterojunction that enhances the lifetime of e^-/h^+ pairs by improving charge separation and expanding the range of excitation of these wide band gap semiconductors in the visible range [102–106]. The coupling between WO_3 and TiO_2 produces surface modifications such as enhanced acidity, increased surface area, various W oxidation states involving oxygen vacancies, and different WO_3 phases that have beneficial effects for photocatalytic and photoelectrocatalytic applications [102–104]. Ramos-Delgado *et al.* prepared WO_3/TiO_2 by the sol-gel method for the photocatalytic degradation of malathion pesticides under solar radiation. Notably, WO_3 (2 wt%)/TiO_2 exhibited the highest photocatalytic performance. This high activity was attributed to the large surface area that enhances the number of active surface sites available and the presence of small nanoclusters of WO_3 (0.8–1.6 nm) on the anatase TiO_2 nanoparticles that work as electron traps, reducing the number of recombination centers on the catalyst [103].

As described in the previous paragraph, the coupling of ZnO, a large band semiconductor (~3.3 eV), with WO_3 improved the absorption of visible light, facilitated the separation of electron-hole pairs, and suppressed the light-induced corrosion of ZnO [105,106]. Moreover, the surface acidity of the mixed oxide was enhanced due to the incorporation of WO_3, facilitating the adsorption of organic pollutants on the catalyst surface [105]. The improved photocatalytic activity of organic pollutants such as diclofenac and 2,4-D herbicide in aqueous media at acidic pH (4.7–6.0) was demonstrated, indicating that the incorporation of WO_3 enhanced the chemical stability of ZnO [105,106].

Other metal oxides, such as In_2O_3, in combination with WO_3, formed the type II heterojunction In_2O_3-WO_3 due to the appropriate band alignment of these materials. The formed composite was designed for the photocatalytic reduction of CO_2 because In_2O_3 is used in gas sensing applications, showing a high affinity towards CO_2. In the composite, WO_3 presented a monoclinic phase, while the phase of In_2O_3 was cu-

bic. The incorporation of WO_3 in In_2O_3 did not modify the particle size; however, the presence of In_2O_3 enhanced the crystallinity and smoothed the particle surface of the mixed oxide. The calculated band potentials of both semiconductors confirmed that the photoreduction of CO_2 into CH_3OH was feasible due to the favorable band position of In_2O_3 and the reduced e^-/h^+ recombination rate [101].

The bismuth-based photocatalyst BiOCl has been described as a promising alternative to metal oxides such as TiO_2 and ZnO to perform the photocatalytic degradation of organic pollutants. However, its wide E_g (~3.1 eV) enables coupling with semiconductors, such as WO_3, necessary, creating a type II heterojunction structure to enhance the performance under visible light irradiation and retard the recombination rate of the photogenerated e^-/h^+ carriers. Thus, the efficient degradation of RhB and tetracycline hydrochloride (TC) under visible light irradiation (λ = 420 nm) was demonstrated using the $WO_3/Bi_{12}O_{17}Cl_2$ composite in a mass ratio of 99.5:0.5. The enhanced performance of the prepared catalyst was attributed to the enlarged specific surface area and favorable morphology, optical properties, and electronic band alignment [107].

WO_3-based heterojunction type II has been considered a suitable photoanode for PEC water splitting since it absorbs a wide range of the solar spectrum (~12%) because of its good electron transport ability (12 cm^2 V^{-1} s^{-1}) [108] and because it can act as a good photocathode protection against corrosion [109,110]. Diverse WO_3-based type II heterostructures have been explored as photoanodes for PEC water splitting, such as WO_3/TiO_2 [104], $WO_3/\alpha Fe_2O_3$ [111], WO_3/NiO [112], WO_3/Cu_2O [113], CoO_x/WO_3 [114], $WO_3/BiVO_4$ [115], WO_3/Bi_2S_3 [116], and $WO_3/CdIn_2S_4$ [117]. Moreover, the coupling of p-type metal oxides such as NiO [112], Cu_2O [113], and CoO_x [114] with n-type WO_3 produces a type II p-n heterojunction that induces the formation of an internal electric field across the interfaces directing from an n-type semiconductor (light absorber) towards the p-type semiconductor catalyst. This built-in electric field promotes charge separation, enhancing the PEC water splitting process. Huang *et al.* described the deposition of CoOx nanoparticles on WO_3 to improve the oxidation selectivity and the Faradaic efficiency for PEC water oxidation [114]. On the other hand, the coupling of WO_3 with semiconductors with narrow band gap values has attracted much attention, including $BiVO_4$ (2.4 eV) [115], Fe_2O_3 (2.2 eV) [111], Bi_2S_3 (1.3 eV) [116], and CdIn2S_4 (2.4 eV) [117], due to the increase in light absorption efficiency and promotion of the separation of charge carriers. The type-II heterojunction $WO_3/BiVO_4$ is a promising photocatalyst to achieve enhanced efficiency of PEC water splitting due to its matched band edge levels, efficient e^-/h^+ pairs separation, and visible light absorption abilities. In the $WO_3/BiVO_4$ photoanode, $BiVO_4$ served as a visible-light absorber (~30% sunlight), and WO_3 functioned as an electron transfer agent [108,115,118]. For example, Lee *et al.* fabricated WO_3-$BiVO_4$ heterojunction photoanodes by using glancing angle deposition of WO_3 (monoclinic phase) aligned at 70° to the fluorine-doped tin oxide (FTO) substrate, allowing a large active surface area. Afterward, via pulsed anodic electrodeposition, the nanodot-like monoclinic $BiVO_4$ conformally covered the surface of WO_3 without blocking the substrate-electrolyte contact (see Fig. 6). This photoanode configuration exhibited improved photoelectrochemical performance under simulated solar light for the water oxidation process [115].

The contact quality at the interface of the heterojunction plays a crucial role in efficient charge separation and transport for PEC water splitting applications. Thus, it is essential to develop a practical and straightforward approach to prepare heterostructured materials. Three-dimensional (3D) WO_3 nanoplate/Bi_2S_3 nanorod heterostructures on FTO substrates were prepared by combining the hydrothermal method, SILAR process, and chemical bath deposition reaction. The 3D WO_3 nanostructure with thin Bi_2S_3 nanorods provided a more direct carrier transport pathway and contact sites with the electrolyte, resulting in an efficient oxygen evolution reaction at the electrode/electrolyte interface. In this way, the type-II heterojunction between WO_3 and Bi_2S_3 effectively promoted the separation of electrons and holes due to Bi_2S_3 being an n-type semiconductor with a narrow E_g (1.3 eV) and high absorption coefficient (10^4–10^5). Bi_2S_3 incorporation extended the absorption wavelength to near-infrared light, leading to less recombination of e^-/h^+ pairs to enhance the photocurrent response and support the injection of photogenerated electrons from Bi_2S_3 to WO_3 [116].

A facile synthesis approach combining the hydrothermal method and chemical bath deposition process was used to prepare the $WO_3/CdIn_2S_4$ composite photoanode. In this design, the small band gap of the n-type semiconductor $CdIn_2S_4$ (2.4 eV) with an appropriate band position enlarged the light absorption range of the photoanode and showed high catalytic activity. Therefore, the fabricated type-II heterojunction between WO_3 and $CdIn_2S_4$ significantly promoted charge separation and transport at the semiconductor interface, leading to enhanced PEC water splitting performance of the $WO_3/CdIn_2S_4$ photoanode [117].

Khampuanbut *et al.* recently described another interesting photocatalytic application reported for WO_3-based type II heterojunctions combining WO_3 and BiOBr. The WO_3/BiOBr heterojunction was prepared by precipitation method exhibiting suitable energy band alignment. The WO_3/BiOBr catalyst showed superior photocatalytic activity compared with pure BiOBr and WO_3 to carry out the selective oxidative coupling of amines to imines under visible light. The enhanced performance of the heterostructured material was related to the increased oxygen vacancy concentration, the effective separation of photogenerated e^-/h^+ pairs, and efficient interfacial charge transfer. For practical application in green synthesis, the WO_3/BiOBr heterojunction system exhibited photostability and recyclability, as demonstrated during four consecutive cycles [97].

In past years, the study of photocatalytic fuel cells (PFCs) has gained significant importance since wastewater treatment and energy recovery can be simultaneously conducted [119–121]. Zeng *et al.* reported an efficient photoanode based on an epitaxial WO_3 nanorod/TiO_2 nanothorn array (TiO_2/WO_3/W) using the arrangement of Scheme 2, which was beneficial in enhancing the separation and transfer of photogenerated e^-/h^+ pairs and worked as inherent atomic-scale protection for the WO_3 photoanode against electrolytic corrosion [120]. This result was attributed to the formation of a highly efficient type II heterojunction promoting the transfer of photogenerated electrons from TiO_2 CB to WO_3, and the holes were transferred from WO_3 VB to TiO_2. Moreover, adding a small amount of ferrous ions into the pollutant solution enhanced the charge transfer and production of hydroxyl radicals, which resulted in the improvement of the degradation efficiency of atrazine (96%) and the high and stable conversion of the organic compound into electricity (power output, 563 mW m^{-2}). These promising results represent a sustainable alternative to simultaneously address the water contamination and the energy supply by using innovative WO_3-based materials. The Table 4 summarizes the overview of the most relevant photocatalytic applications using WO_3-based type-II heterojunction photocatalysts.

Z-scheme systems

Despite the improved charge separation and transport efficiencies attained by type II heterojunctions, the redox capability of the system is sacrificed during the process at the same time since photogenerated electrons and holes are transferred to CB and VB with lower reduction and oxidation potentials, respectively [123–125]. In this context, to overcome this disadvantage, the Z-scheme mechanism was proposed in 1979 by Bard, mimicking the natural photosynthetic process [126]. To date, three generations of Z-scheme photocatalyst systems have been developed over the last 30 years (see Fig. 7), namely, the mediated Z-scheme [96], all solid-state Z-scheme (ASS) [127] and direct Z-scheme [128]. WO_3-based catalysts have been of paramount importance since they were the first developed visible light-responsive Z-scheme [129].

The mediated Z-scheme consists of the coupling of two photocatalytic semiconductors and a liquid redox mediator such as Fe^{2+}/Fe^{3+}or IO_3^-/I^- [130]. In this system, the coupled materials are not in physical contact, but the redox pair acts as a bridge between them. Oxidation

Table 4
The overview of photocatalytic applications using WO_3 based heterojunctions type II.

Photocatalyst	Synthesis method	Application	Experimental conditions	Results	Ref
WO_3/TiO_2	Sol-gel	Malathion degradation	250 mg catalyst in 250 mL of an aqueous solution of malathion (12 mg L^{-1}). Natural sunlight	76% of TOC removal in 300 min using 2 wt% WO_3/TiO_2	[103]
$WO_3 \bullet H_2O/TiO_2$	Solvothermal	MO degradation	50 mg catalyst and 80 mL MO solution (20 mg L^{-1}). 300 W Xe lamp (λ=300–1100 nm)	95.5% of MO degradation in 150 min of reaction using $TiO_2/WO_3 \bullet H_2O$ (Ti/W 95:5)	[122]
WO_3/TiO_2	Hydrothermal	PEC Water splitting	A standard three-electrode cell in 0.5 M Na_2SO_4, WO_3/TiO_2 working electrode, SCE, and Pt wire as a reference and counter electrodes, respectively. 500 W Xe lamp (λ= 300–1100)	The WO_3 (40 wt%) /TiO_2film presented the highest photocurrent density of 210 μA cm^{-2} at 0.75 V *vs.* Ag/AgCl	[104]
WO_3/ZnO	Hydrothermal	Diclofenac degradation	0.8 g L^{-1} of photocatalyst in diclofenac aqueous solution (20 mg L^{-1}). 400 W Metal halide lamp (λ= 583 nm)	76% of TOC removal was using WO_3/ZnO (10:1)	[105]
WO_3/ZnO	Hydrothermal / deposition	2,4-D degradation	100 mg of catalyst in 100 mL of 2,4-D aqueous solution (20 mg L^{-1}). Natural sunlight	91.7% degradation after 7 min, with WO_3/ZnO (2% W/Zn)	[106]
$WO_3/Bi_{12}O_{17}Cl_2$	Hydrothermal	RhB and TC degradation	80 mg of photocatalysts in 80 mL of the aqueous solution of RhB (20 mg L^{-1}) or TC (20 mg L^{-1}). 300 W Xe lamp (λ=420–780 nm)	100% of RhB degradation and 65% of TC degradation with $WO_3/Bi_{12}O_{17}Cl_2$ (99.5:0.5)	[107]
WO_3/In_2O_3	Precipitation	Photocatalytic reduction of CO_2 into CH_3OH	The high purity CO_2 gas (99.99%) was purged into 100 mL water containing WO_3/In_2O_3. Pulsed laser (λ=355 nm)	Methanol yield of 496 μmol g^{-1} h^{-1} and the quantum efficiency of 2.25%	[101]
WO_3@α-Fe_2O_3	Hydrothermal, precipitation, spin coating and calcination	PEC Water splitting	A standard three-electrode cell in 0.5 M Na_2SO_4, WO_3@α-Fe_2O_3 working electrode, SCE, and Pt wire as a reference and counter electrodes, respectively. 500 W Xe lamp (λ= 300 – 1100)	Photocurrent response of 1.66 mA cm^2, IPCE of ~73.7% at 390 nm, and excellent photostability of 100% at 1.23 V versus RHE	[111]
CoOx/WO_3	Hydrothermal	PEC Water splitting	A standard three-electrode cell in 0.1 M K_3PO_4, CoOx/WO_3 working electrode, Ag/AgCl, and Pt plate as a reference and counter electrodes, respectively. 500 W Xe lamp (λ= 300–1100)	Enhanced Faradaic efficiency using CoOx/WO_3 electrode (92.1%)	[114]
NiO/WO_3	Hydrothermal	PEC Water splitting	A standard three-electrode cell in NaOH/KH_2PO_4, NiO/WO_3 working electrode, Ag/AgCl, and Pt foil as a reference and counter electrodes, respectively. 500 W Xe lamp (λ= 300–800)	Photocurrent density –23.39 μA cm^{-2} at 1.20 V *vs.* RHE under using NiO/WO_3	[112]
WO_3 NRs/Cu_2O	Hydrothermal – electrodeposition	PEC Water splitting	A standard three-electrode cell in 0.1 M H_2SO_4, NiO/WO_3 working electrode, Ag/AgCl, and Pt foil as a reference and counter electrodes, respectively. 500 W Xe lamp (λ= 300 – 800)	Photocurrent density 1.37 mA cm^{-2} at 0.8 V *vs.* RHE	[113]
$WO_3/BiVO_4$	Deposition - electrodeposition	PEC Water splitting	A standard three-electrode cell in 0.1 M K_3PO_4, $WO_3/BiVO_4$ working electrode, Ag/AgCl, and Pt mesh as a reference and counter electrodes, respectively. 500 W Xe lamp (λ= 300 – 1100)	Photocurrent density of 4.55 mA cm^{-2} and IPCE of 80% at 1.23 V *vs.* RHE	[115]
WO_3/Bi_2S_3	Hydrothermal	PEC Water splitting	A standard three-electrode cell in 0.1 M Na_2S/0.1 M Na_2SO_3, WO_3/Bi_2S_3 working electrode, Ag/AgCl, and Pt mesh as a reference and counter electrodes, respectively. 500 W Xe lamp (λ= 300–1100).	Photocurrent of 5.95 mA cm^{-2} at 0.9 V *vs.* RHE using WO_3/Bi_2S_3 with seed layer	[116]
$WO_3/CdIn_2S_4$	Hydrothermal – chemical bath deposition	PEC Water splitting	A standard three-electrode cell in 0.25 M Na_2SO_3, $WO_3/CdIn_2S_4$ working electrode, Ag/AgCl, and Pt mesh as a reference and counter electrodes, respectively. 500 W Xe lamp (λ= 300–1100).	Photocurrent of 1.06 mA cm^{-2}at 1.23 V versus RHE using $WO_3/CdIn_2S_4$	[117]
WO_3/BiOBr	Precipitation method	Oxidative coupling of amine to imine compounds	100 mg of photocatalyst, 0.125 mmol benzylamine, 10 mL of acetonitrile, and o-dichlorobenzene (internal standard). 50 W cold white light-emitting diode (λ= 432 nm)	The rate constant for the oxidative coupling of benzylamine in WO_3/BiOBr was 2.4 and 2.1 times higher than that in WO_3 and BiOBr, respectively	[97]
TiO_2/WO_3/W	Hydrothermal – chemical bath deposition	Photocatalytic Fuel cell	Dual electrode configuration, 10 mg L^{-1} atrazine solution, 0.1 M K_2SO_4 electrolyte, adding 2 mM $FeSO_4$ for enhanced PFC. 500 W Xe lamp (λ= 300–1100)	The current densities were 3734 mA m^{-2} (short-circuit) and 563 mW m^{-2} (maximum power output) allowing 96% of atrazine degradation with high reusability	[120]

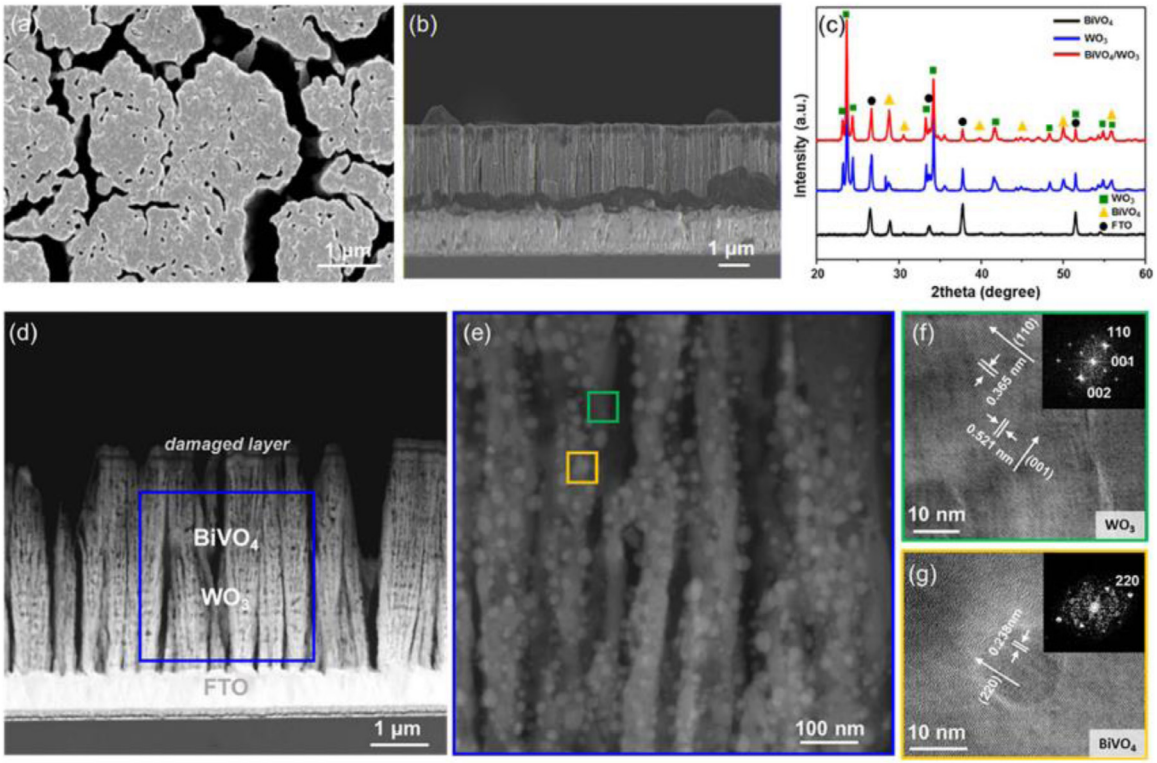

Fig. 6. (a), (b) Top and cross-section FESEM images of the optimum $BiVO_4$/70°-WO_3 nanorods, (c) X-ray diffraction patterns of $BiVO_4$ (black line), WO_3 nanorods (blue line), $BiVO_4$/70°- WO_3 nanorods (redline), (d) Corresponding TEM images of $BiVO_4$/70°-WO_3 nanorods, (e) Expanded image of $BiVO_4$/WO_3 nanorods, (f) (110), (001), and (002) of 70°-WO_3 nanorods, and (g) Small square by HRTEM showing crystalline planes of (220) of $BiVO_4$ (from [115]).

and reduction reactions occur in each photocatalyst with the highest oxidation or reduction potential, respectively, and the redox couple works as an acceptor or donor, depending on the photosystem. WO_3 is usually employed as an oxidation photosystem (OPS) because of the highly positive potential of its VB (~2.83 – 3.22 V) [117,131,132].

For the first time, in 2001, Sayama *et al.* used a WO_3-based catalyst to construct a Z-scheme system composed of Pt-WO_3 and Pt-$SrTiO_3$(Cr-Ta-doped) photocatalysts and IO_3^-/I^- as a redox mediator for visible light water splitting to produce H_2 [129]. Stoichiometric water splitting into H_2 and O_2 ($H_2/O_2 = 2$) was reported for the first time using this Z-scheme. Similarly, Miseki *et al.* used surface-treated PtO_x/WO_3 as an O_2 evolution photocatalyst in the presence of IO_3^- or I_3^- ions as redox mediators. It was found that the photocatalytic performance of the Z-scheme strongly depends on two conditions: the nature of the redox couple and its interaction with the photocatalyst surface. PtO_x/WO_3 without surface treatment showed negligible photocatalytic activity when

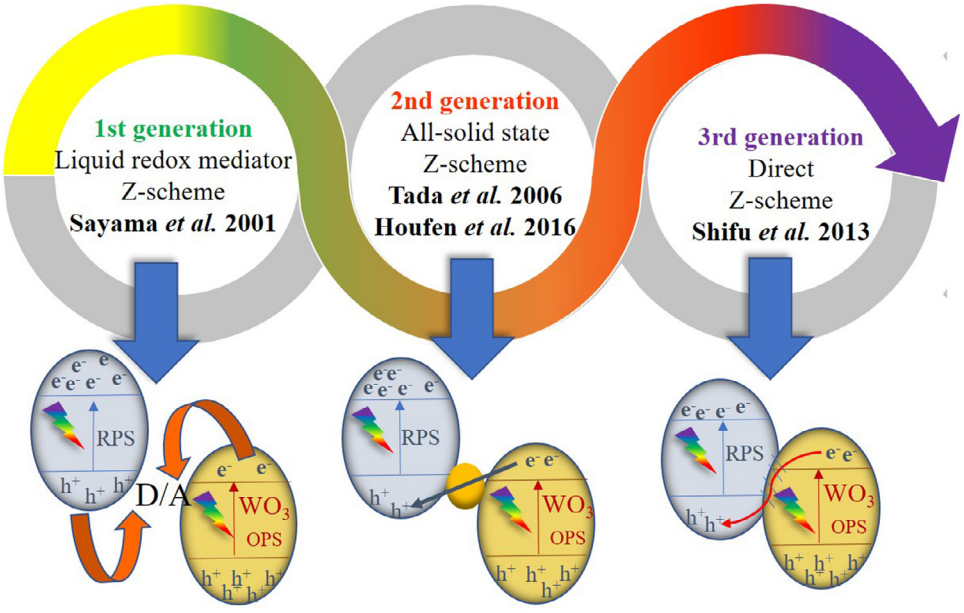

Fig. 7. Timeline of WO_3-based Z-scheme photocatalysts, *OPS=oxidation photosystem, and *RPS= reduction photosystem [96,128,134,136].

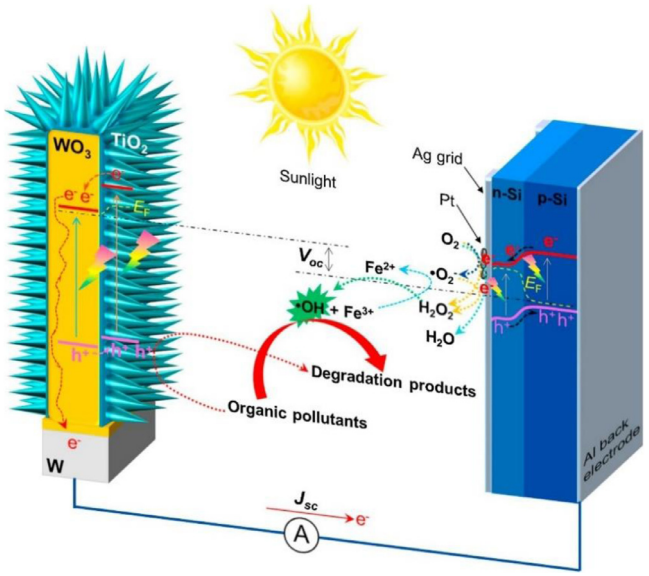

Scheme 2. Diagram of the TiO_2/WO_3/W photoanode and the possible mechanism of the PFC for simultaneous wastewater treatment and energy recovery under solar radiation (from [120]).

the I_3^- ion was used as a redox mediator, while high O_2 evolution was yielded with surface treatment, which explains the synergistic effect between the surface properties and redox couple. However, the concentration of the redox mediator used in this kind of Z-scheme represents the main drawback of this system. An optimal concentration must be determined since a high concentration could cause undesirable backward reactions and thus reduce the overall efficiency [133]. To avoid inconvenience with handling liquid redox mediators, the second generation of the Z-scheme, the ASS Z-scheme, was proposed in 2006 by Tada *et al.* [134].

In this second generation, the liquid redox couple was replaced by a solid electron mediators (SEMs), which eliminated the drawback of backward reactions. Metals are known as the main SEMs because of their outstanding conductive properties and because they can also act as cocatalysts to enhance photocatalytic performance [98,123,127,135]. The SEMs play an essential role in the charge transfer in the ASS Z-scheme; hence, it must be chosen carefully. This system was first used by Houfen *et al.* in 2016 to improve WO_3 performance when it was combined with g-C_3N_4. They described the effect of the Fermi energy level of the electron mediator (Ag, Cu, Au) to determine an adequate SEMs according to the energy band theory [136]. The contact of the junction between semiconductors and SEMs is a critical factor because the migration of charge carriers depends on band bending by the Fermi energy level difference. If the Fermi energy level of the semiconductor is above the SEMs, the band bends upward because of the depletion of charges and vice versa. Therefore, it is preferred to choose SEMs with a Fermi energy level between those of each semiconductor used in the Z-scheme system.

Silver nanoparticles are one of the most commonly used SEMs, and these NPs have been used in systems composed of WO_3 and Ag_3PO_7 [127], Ag_2CO_3 [123], and Ag_2WO_4 [137], showing high photocatalytic efficiency for aqueous pollutant degradation. Other SEMs that have attracted attention in recent years are graphene materials such as reduced graphene oxide (RGO) or graphene oxide (GO) and carbon nanodots. These SEMs represent a very suitable alternative to noble metals because they show high electron mobility and lower cost. For example, Zeng *et al.* reported an ASS Z-scheme TiO_2/RGO/WO_3 that was evaluated in water disinfection by the inactivation of *Escherichia coli* (*E. coli*), as shown in Fig. 8 [138].

The authors demonstrated that the photocatalytic performance of the ASS Z-scheme was superior to that of the simple TiO_2/WO_3 heterojunction, since the addition of RGO highly promoted electron migration and the production of reactive oxygen species (ROS) such as H_2O_2, acting as a co-catalyst during the process. Similarly, Li *et al.* reported the synthesis of ASS Z-scheme WO_3/RGO/MoS_2 and its application in water decontamination [139]. High dispersion of WO_3 and MoS_2 particles over the RGO nanosheets was observed, which enhanced the contact area between both semiconductors. The graphene materials show outstanding conductivity and electron mobility, which makes them good candidates for excellent SEMs.

Despite the excellent behavior of ASS Z-scheme generation, it is well known that the incorporation of noble metals or even conductive materials such as GO is associated with high cost, and photocatalyst stability remains unsolved. Therefore, obtaining mediator-free systems is desirable for practical applications. Thus, Wang *et al.* in 2016 defined the term redox-mediator-free Z-scheme fabricating the AgI/WO_3 photocatalyst [140]. This system, commonly called a direct Z-scheme, corresponds to the third generation, which is composed of two photosystems, and charge migration occurs through the interface formed by an intimate junction between both catalysts (Fig. 9).

Since this concept was first developed, it has been intensively investigated by several research groups to combine WO_3 with metal-free compounds such as g-C_3N_4 [141] and carbon nanodots [131,142], metal oxides [99,143–145] and different chalcogenides [22,130,146,147]. The formation of a direct Z-scheme is determined by the electronic structure of the constituent semiconductors and the synthesis method. Jin *et al.* reported the synthesis of a hierarchical Z-scheme CdS-WO_3. The hierarchical structure in WO_3 particles is beneficial for the contact area between both semiconductors and the adsorption of CO_2. The Z-scheme not only improved the separation efficiency but also induced WO_3 activity for the CO_2 reduction process, enhancing the catalytic activity in a synergistic process [146].

Material characterization is a crucial step in understanding the improvements in photocatalytic performance. In this sense, different authors have proposed a combination of experimental and theoretical techniques to provide a reasonable explanation of the enhancements reported for direct Z-scheme photocatalysts [146,148–150]. In addition to conventional analytical techniques, such as XRD, FESEM, TEM, electrochemical and photoelectrochemical tests such as Mott-Schottky analysis, transient photocurrent response and electrochemical impedance spectroscopy (EIS) have been extensively used to demonstrate improved characteristics such as high charge separation and transfer rate, which correspond to the performance of direct Z-scheme heterojunctions [124,140]. Additionally, density-functional theory (DFT) calculations are useful to understand the transfer mechanism and interfacial properties that allow researchers to propose the involved mechanisms for e^-/h^+ pair transfer through the interface [151–153].

Over the last two years, scientific efforts have been focused on improving the photocatalytic efficiency of the direct Z-scheme by two methods, combining the SPR effect and double Z-scheme heterojunctions [99,143,154–158]. Noble metals loaded on the heterojunction provide a strong SPR effect that can further enhance the separation efficiency of e^-/h^+ pairs. Silver and platinum nanoparticles have been reported as useful cocatalysts with SPR effects in direct Z-scheme WO_3-based photocatalysts [143,156,159,160]. Zhou *et al.* reported the synthesis of a Ag/WO_3/Bi_2WO_6 SPR Z-scheme and its photocatalytic evaluation in the degradation of VOCs in the gaseous phase [156]. The authors described that the 2 wt% Ag-WO_3/Bi_2WO_6 photocatalyst showed 1.8- and 2.8-times higher visible-light degradation rates than WO_3/Bi_2WO_6 and Bi_2WO_6, respectively, which were attributed to the improved separation efficiency and utilization of photoinduced e^-/h^+ pairs. Meanwhile, Gong *et al.* affirmed that Pt nanoparticles could act as electron traps, improving the lifetime of photogenerated electrons, as demonstrated in the water-splitting process under visible light, yielding

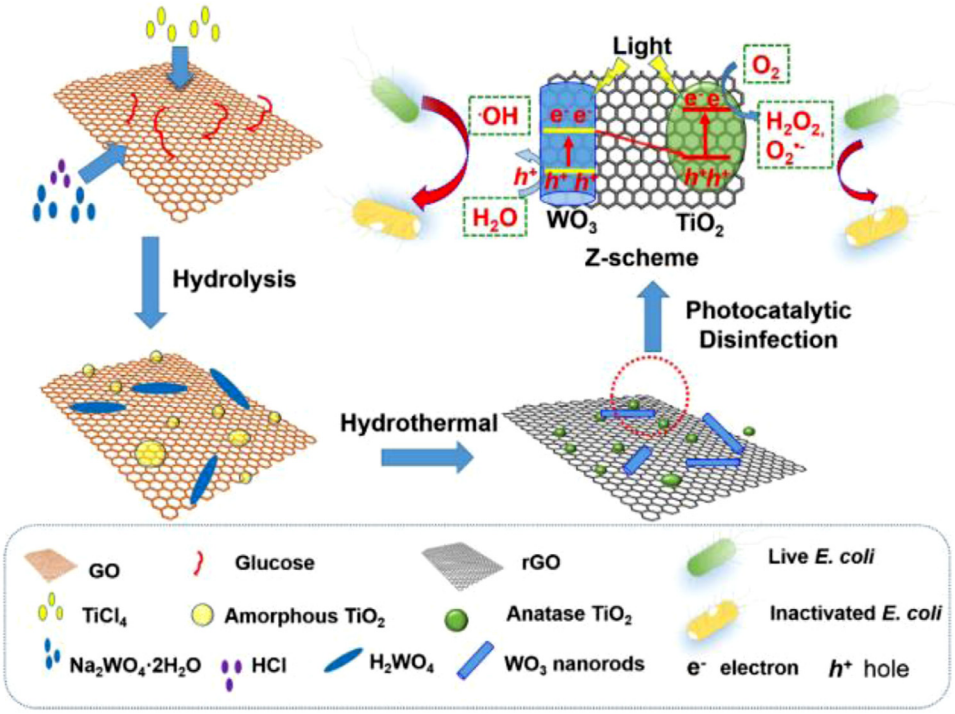

Fig. 8. Illustration of the synthesis process of TiO_2/RGO/WO_3 ASS Z-scheme and its application on water disinfection (from [138]).

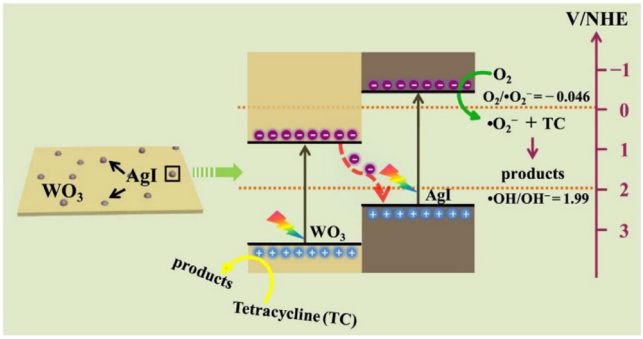

Fig. 9. The possible photocatalytic mechanism for the degradation of TC on the direct Z-scheme AgI/WO_3 photocatalyst (from [140]).

an O_2 evolution rate almost 1.6 times higher than that of Pt@Cu_2O/WO_3 [159].

Similarly, nonmetals have also been incorporated on heterojunctions to generate a Z-scheme WO_3 system. In a recent work, Huang *et al.* prepared N-WO_3 coupled with Ce_2S_3 to obtain N-WO_3/Ce_2S_3 nanotubes immobilized on carbon textiles for formaldehyde and phenol degradation. They reported that nitrogen-doped WO_3 (N-WO_3) and the heterojunction WO_3/Ce_2S_3 exhibited superior activity compared to bare WO_3, achieving 50 and 70% HCHO conversion, respectively, in 120 min. However, complete conversion of formaldehyde was obtained with the nonmetal-doped heterojunction N-WO_3/Ce_2S_3 in 80 min under visible light. This removal was three times higher than that found with bare WO_3, which only degraded 40% of HCHO in 120 min. Similar behavior was observed when the degradation and mineralization of phenol was conducted with WO_3, N-WO_3 and N-WO_3/Ce_2S_3 catalysts, where 50, 80 and 99% phenol removal was attained, respectively. Furthermore, 94% TOC abatement was reached with N-WO_3/Ce_2S_3 nanotubes, indicating complete mineralization of phenol. This result was attributed to the strong electronic interaction between N-WO_3 and Ce_2S_3, which was beneficial for the charge carrier dynamics and hence for improving the photocatalytic performance. Additionally, electrochemical impedance spectra (EIS) measurements, photocurrent transient profiles, and PL studies showed that the N-WO_3/Ce_2S_3 photocatalyst exhibits the most efficient separation of photogenerated charges and a lower rate of e^-/h^+ recombination. Electron spin resonance (ESR) studies and the band edge position calculated using hybrid density functional theory (DFT) analysis indicated that the enhanced photocatalytic performance was ascribed to the Z-scheme mechanism (Fig. 10) [161].

On the other hand, the dual Z-scheme is a ternary photocatalyst in which two linked Z-scheme transfer patterns coexist to further enhance the separation efficiency and visible light absorption ability [154,157]. In this context, this kind of photosystem has been used for different environmental applications, such as H_2 production, pollutant degradation [157], air decontamination [162], and CO_2 photoreduction [163]. A ternary $BiFeO_3$-g-C_3N_4-WO_3 system (Scheme 3) was synthesized and used for pollutant degradation and photocatalytic water splitting [157].The authors reported that the ternary heterojunction under visible-light irradiation showed 63% 2,4-dichlorophenol (2,4-DCP) degradation and 90 μmol h^{-1} g^{-1} H_2 evolution, resulting in 2.2 and 90 times higher than that of pure WO_3, respectively. Ma *et al.* reported the ternary heterojunction WO_3/NiS_2/$NiGa_2O_4$, in which NiS_2 was used as a conductive pathway between the other two semiconductors due to its matched CB and VB levels with those of WO_3 and $NiGa_2O_4$, respectively. When the dual Z-scheme was used under optimal experimental conditions under simulated solar light in aqueous media, the conversion of NO_2^- and SO_3^{2-} reached 87.03% and 97.47%, respectively [162]. Meanwhile, visible light CO_2 photoreduction towards CO as the major product was reported using the WO_3-TiO_2/Cu_2ZnSnS_4 dual Z-scheme [163]. The enhanced CO/CH_4 production (15.37/1.69 μmol h^{-1} g^{-1}) was attributed to the higher surface area, the strong absorption in the visible region, and the improved separation efficiency of the e^-/h^+ pairs due to the dual heterojunction.

Conclusions and perspectives

In this critical review, the adaptability of visible-light responsive WO_3 semiconductors with other materials was demonstrated. The properties of this metal oxide have been exploited to propose numerous WO_3-based photocatalysts with application in the remediation of the

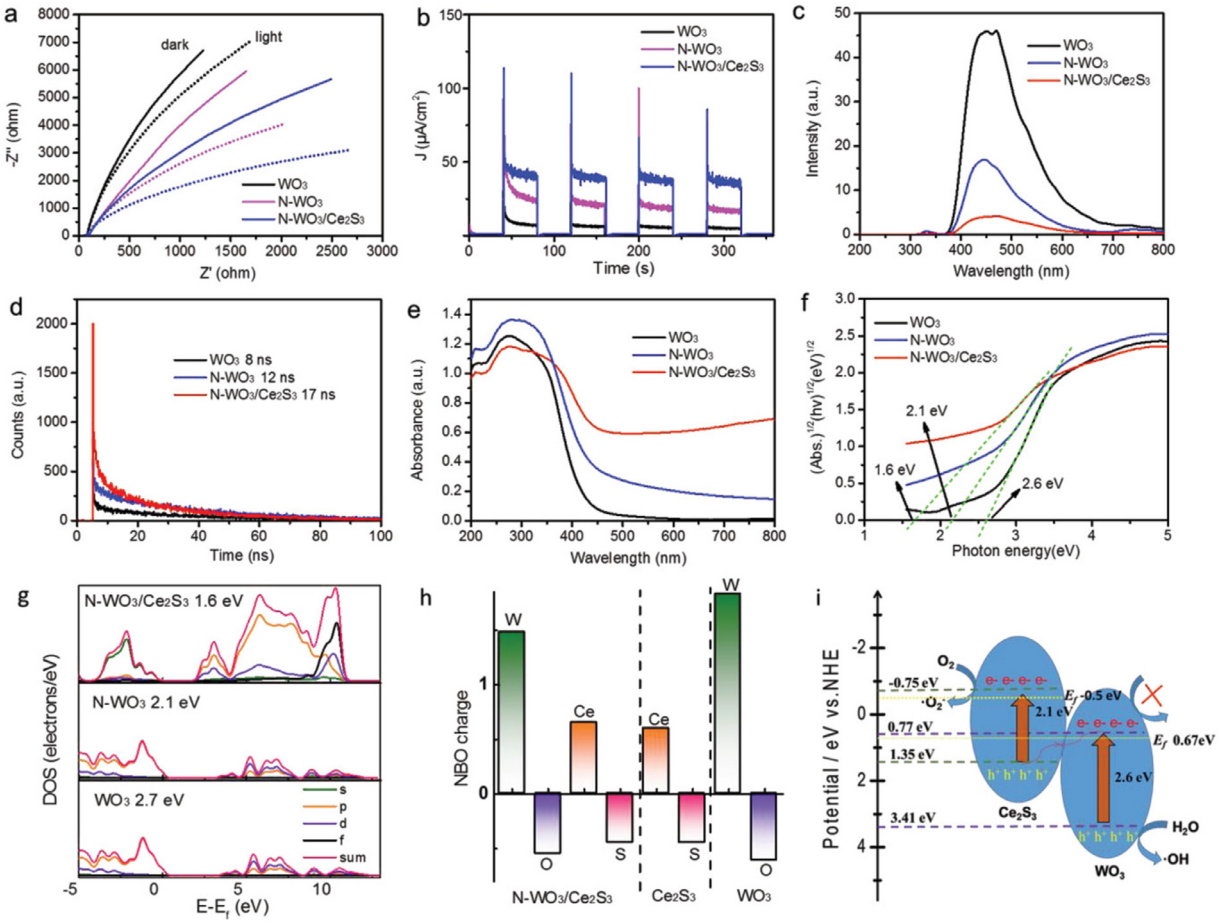

Fig. 10. a) EIS Nyquist plots, b) photocurrents responses, c) photoluminescence spectra with 320 nm excitation wavelength and d) time-resolved photoluminescence spectra of WO_3, N-WO_3, and N-WO_3/Ce_2S_3 NBs. e) UV–vis diffuse reflectance spectra of WO_3, N-WO_3, and N-WO_3/Ce_2S_3 NBs. f) Optical bandgaps determined from the UV–vis diffuse reflectance spectra. g,h) Calculated DOS of N-WO_3/Ce_2S_3 NBs. i) Z-scheme charge separation in photocatalytic systems. Condition: under visible light irradiation (from [161]).

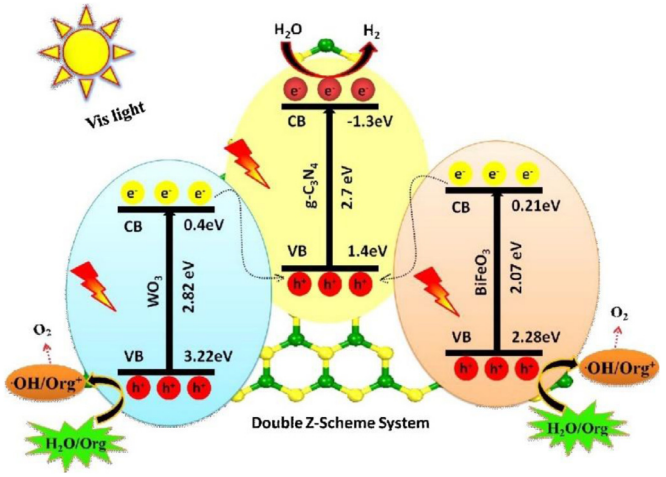

Scheme 3. Representation of the energy diagram, charge transfer mechanism, and the photocatalytic processes over $BiFeO_3$-g-C_3N_4-WO_3 composite under visible-light irradiation (from [157]).

environment or energy production using visible o solar light as activation source. A variety of strategies to improve the response of WO_3 with efficient charge carrier separation was reviewed. A brief description of the main achievements using tungsten oxide-based photocatalysts was provided, and the most novel advances were discussed. The feasibility of WO_3 to absorb photons of low energy and its capacity to combine with many semiconductor materials allows the development of visible light WO_3-based photocatalysts for different environmental applications.

Although the studied materials based on WO_3 have demonstrated excellent performance as photocatalysts under visible or solar light at the laboratory scale, there are still some crucial aspects that need to be considered for practical applications. More studies are necessary to ensure the stability and nontoxicity of the prepared materials. Moreover, leaching tests should be performed to evaluate the stability and lack of lixiviation of the components when these materials are tested for water treatment. Tungsten oxide is a nontoxic material, but few studies have been conducted to investigate the toxicity of prepared WO_3 combined with other materials for photocatalytic applications.

Additionally, the photoreactor design and how to suspend or support the catalyst are key aspects that must be considered for efficient photocatalytic applications on a large scale. It is well known that reactor design is different when artificial visible light from lamps is used compared to natural sunlight application. The challenge is to combine the engineering aspects of photocatalytic technology and toxicity and recycling studies of prepared materials with the fundamental features of WO_3-based photocatalytic materials.

Therefore, there is still work to be done, but the scientific community is getting closer to developing green technologies based on more active and efficient photocatalytic materials under visible light. The WO_3-based photocatalysts represent an attractive alternative for the reduction

of the pollutants in the environment and the production of fuels using a low-cost energy source as the solar light.

Declaration of Competing Interest

The authors declare that they have no known competing financial interests or personal relationships that could have appeared to influence the work reported in this paper.

Acknowledgments

The authors give thanks to the National Council of Science and Technology of Mexico (CONACyT) through the project number A1-S-40260 and PAICyT program from the Universidad Autonoma de Nuevo Leon (grant CE1291-20) for the funding. J. Murillo-Sierra thanks to CONACyT for the doctoral scholarship.

References

[1] S. Rani, N. Bao, S.C. Roy, Solar spectrum photocatalytic conversion of CO_2 and water vapor into hydrocarbons using TiO_2 nanoparticle membranes, Appl. Surf. Sci. 289 (2014) 203–208, doi:10.1016/j.apsusc.2013.10.135.

[2] N.A. Ramos-Delgado, L. Hinojosa-Reyes, I.L. Guzman-Mar, M.A. Gracia-Pinilla, A. Hernández-Ramírez, Synthesis by sol-gel of WO_3/TiO_2 for solar photocatalytic degradation of malathion pesticide, Catal. Today 209 (2013) 35–40, doi:10.1016/j.cattod.2012.11.011.

[3] S. Agarwal, Y.K. Prajapati, Design of broadband absorber using 2-D materials for thermo-photovoltaic cell application, Opt. Commun. 413 (2018) 39–43, doi:10.1016/j.optcom.2017.12.030.

[4] H. Huang, Y. Li, M. Wang, W. Nie, W. Zhou, E.D. Peterson, J. Liu, G. Fang, D.L. Carroll, Photovoltaic-thermal solar energy collectors based on optical tubes, Sol. Energy 85 (2011) 450–454, doi:10.1016/j.solener.2010.12.011.

[5] J.C. Murillo-Sierra, E. Ruiz-Ruiz, L. Hinojosa-Reyes, J.L. Guzmán-Mar, F. Machuca-Martínez, A. Hernández-Ramírez, Sulfamethoxazole mineralization by solar photo electro-Fenton process in a pilot plant, Catal. Today (2017) 1–7, doi:10.1016/j.cattod.2017.11.003.

[6] E.J. Ruiz, A. Hernández-Ramírez, J.M. Peralta-Hernández, C. Arias, E. Brillas, Application of solar photoelectro-Fenton technology to azo dyes mineralization: effect of current density, Fe^{2+} and dye concentrations, Chem. Eng. J. 171 (2011) 385–392, doi:10.1016/j.cej.2011.03.004.

[7] A. Khanna, V.K. Shetty, Solar light induced photocatalytic degradation of reactive blue 220 (RB-220) dye with highly efficient Ag@TiO_2 core-shell nanoparticles: a comparison with UV photocatalysis, Sol. Energy 99 (2014) 67–76, doi:10.1016/j.solener.2013.10.032.

[8] D. Nasuhoglu, V. Yargeau, D. Berk, Photo-removal of sulfamethoxazole (SMX) by photolytic and photocatalytic processes in a batch reactor under UV-C radiation (λ_{max}=254nm), J. Hazard. Mater. 186 (2011) 67–75, doi:10.1016/j.jhazmat.2010.10.080.

[9] A. Priyadharsan, V. Vasanthakumar, S. Karthikeyan, V. Raj, S. Shanavas, P.M. Anbarasan, Multi-functional properties of ternary CeO_2/SnO_2/rGO nanocomposites: visible light driven photocatalyst and heavy metal removal, J. Photochem. Photobiol. A Chem. 346 (2017) 32–45, doi:10.1016/j.jphotochem.2017.05.030.

[10] I. Jansson, K. Kobayashi, H. Hori, B. Sánchez, B. Ohtani, S. Suárez, Decahedral anatase titania particles immobilized on zeolitic materials for photocatalytic degradation of VOC, Catal. Today 287 (2017) 22–29, doi:10.1016/j.cattod.2016.11.041.

[11] X. Yang, H. Cai, M. Bao, J. Yu, J. Lu, Y. Li, Insight into the highly efficient degradation of PAHs in water over graphene oxide/Ag_3PO_4 composites under visible light irradiation, Chem. Eng. J. 334 (2018) 355–376, doi:10.1016/j.cej.2017.09.104.

[12] M. Tahir, Photocatalytic carbon dioxide reduction to fuels in continuous flow monolith photoreactor using montmorillonite dispersed Fe/TiO_2 nanocatalyst, J. Clean. Prod. 170 (2018) 242–250, doi:10.1016/j.jclepro.2017.09.118.

[13] J. Chen, F. Xin, H. Nui, C.-J. Mao, J.-.M. Song, Photocatalytic reduction of CO_2 with methanol over Bi_2S_3-$ZnIn_2S_4$ nanocomposites, Mater. Lett. 1600330 (2017) 1–9, doi:10.1002/crat.201600330.

[14] Y. He, L. Zhang, M. Fan, X. Wang, M.L. Walbridge, Q. Nong, Y. Wu, L. Zhao, Z-scheme SnO_2-x/g-C_3N_4 composite as an efficient photocatalyst for dye degradation and photocatalytic CO_2 reduction, Sol. Energy Mater. Sol. Cells 137 (2015) 175–184, doi:10.1016/j.solmat.2015.01.037.

[15] M.L. Ovcharov, A.M. Mishura, N.D. Shcherban, S.M. Filonenko, V.M. Granchak, Photocatalytic reduction of CO_2 using nanostructured Cu_2O with foam-like structure, Sol. Energy 139 (2016) 452–457, doi:10.1016/j.solener.2016.10.010.

[16] B.S. Kwak, K. Vignesh, N.K. Park, H.J. Ryu, J.I. Baek, M. Kang, Methane formation from photoreduction of CO_2 with water using TiO_2 including Ni ingredient, Fuel 143 (2015) 570–576, doi:10.1016/j.fuel.2014.11.066.

[17] M. Qamar, M.A. Gondal, Z.H. Yamani, Removal of Rhodamine 6G induced by laser and catalyzed by Pt/WO_3 nanocomposite, Catal. Commun. 11 (2010) 768–772, doi:10.1016/j.catcom.2010.02.012.

[18] X. Zeng, Z. Wang, G. Wang, T.R. Gengenbach, D.T. McCarthy, A. Deletic, J. Yu, X. Zhang, Highly dispersed TiO_2nanocrystals and WO_3 nanorods on reduced graphene oxide: z-scheme photocatalysis system for accelerated photocatalytic water disinfection, Appl. Catal. B: Environ. 218 (2017) 163–173, doi:10.1016/j.apcatb.2017.06.055.

[19] R. Nagarjuna, S. Challagulla, P. Sahu, S. Roy, R. Ganesan, Polymerizable sol–gel synthesis of nano-crystalline WO_3 and its photocatalytic Cr(VI) reduction under visible light, Adv. Powder Technol. 28 (2017) 3265–3273, doi:10.1016/j.apt.2017.09.030.

[20] B. Ahmed, S. Kumar, A.K. Ojha, P. Donfack, A. Materny, Facile and controlled synthesis of aligned WO_3 nanorods and nanosheets as an efficient photocatalyst material, Spectrochim. Acta – Part A Mol. Biomol. Spectrosc. 175 (2017) 250–261, doi:10.1016/j.saa.2016.11.044.

[21] C. Wang, X. Li, C. Feng, Y. Sun, G. Lu, Nanosheets assembled hierarchical flower-like WO_3 nanostructures: synthesis, characterization, and their gas sensing properties, Sens. Actuators B: Chem. 210 (2015) 75–81, doi:10.1016/j.snb.2014.12.020.

[22] C. Song, X. Wang, J. Zhang, X. Chen, C. Li, Enhanced performance of direct Z-scheme CuS-WO_3 system towards photocatalytic decomposition of organic pollutants under visible light, Appl. Surf. Sci. 425 (2017) 788–795, doi:10.1016/j.apsusc.2017.07.082.

[23] R. Malik, P.S. Rana, V.K. Tomer, V. Chaudhary, S.P. Nehra, S. Duhan, Nano gold supported on ordered mesoporous WO_3/SBA-15 hybrid nanocomposite for oxidative decolorization of azo dye, Microporous Mesoporous Mater. 225 (2016) 245–254, doi:10.1016/j.micromeso.2015.12.013.

[24] W. Mu, X. Xie, X. Li, R. Zhang, Q. Yu, K. Lv, H. Wei, Y. Jian, Characterizations of Nb-doped WO_3 nanomaterials and their enhanced photocatalytic performance, RSC Adv. 4 (2014) 36064, doi:10.1039/C4RA04080E.

[25] S. Singh, V.C. Srivastava, S.L. Lo, Surface modification or doping of WO_3 for enhancing the photocatalytic degradation of organic pollutant containing wastewaters: a review, Mater. Sci. Forum 855 (2016) 105–126, doi:10.4028/www.scientific.net/MSF.855.105.

[26] M.B. Tahir, G. Nabi, M. Rafique, N.R. Khalid, Nanostructured-based WO_3 photocatalysts: recent development, activity enhancement, perspectives and applications for wastewater treatment, Int. J. Environ. Sci. Technol. 14 (2017) 2519–2542, doi:10.1007/s13762-017-1394-z.

[27] G. Xin, W. Guo, T. Ma, Effect of annealing temperature on the photocatalytic activity of WO_3 for O2 evolution, Appl. Surf. Sci. 256 (2009) 165–169, doi:10.1016/j.apsusc.2009.07.102.

[28] M. Farhadian, P. Sangpout, G. Hosseinzadeh, Morphology dependent photocatalytic activity of WO_3 nanostructures, J. Energy Chem. 24 (2015) 171–177, doi:10.1016/S2095-4956(15)60297-2.

[29] A.M. Mohamed, S.A. Shaban, H.A. El Sayed, B.E. Alanadouli, N.K. Allam, Morphology-photoactivity relationship: WO_3 nanostructured films for solar hydrogen production, Int. J. Hydrogen Energy 41 (2016) 866–872, doi:10.1016/j.ijhydene.2015.09.108.

[30] Y. Liu, Y. Li, W. Li, S. Han, C. Liu, Photoelectrochemical properties and photocatalytic activity of nitrogen-doped nanoporous WO_3 photoelectrodes under visible light, Appl. Surf. Sci. 258 (2012) 5038–5045, doi:10.1016/j.apsusc.2012.01.080.

[31] F. Mehmood, J. Iqbal, T. Jan, A. Gul, Q. Mansoor, R. Faryal, Structural, photoluminescence, electrical, anti cancer and visible light driven photocatalytic characteristics of Co doped WO_3 nanoplates, Vib. Spectrosc. 93 (2017) 78–89, doi:10.1016/j.vibspec.2017.09.005.

[32] P. Praus, L. Svoboda, R. Dvorský, M. Reli, M. Kormunda, P. Mančík, Synthesis and properties of nanocomposites of WO_3 and exfoliated g-C_3N_4, Ceram. Int. 43 (2017) 13581–13591, doi:10.1016/j.ceramint.2017.07.067.

[33] C. Dong, R. Zhao, L. Yao, Y. Ran, X. Zhang, Y. Wang, A Review on WO_3 Based Gas Sensors: Morphology Control and Enhanced Sensing Properties, Elsevier B.V., 2020, doi:10.1016/j.jallcom.2019.153194.

[34] M.B. Tahir, S. Ali, M. Rizwan, A review on remediation of harmful dyes through visible light-driven WO_3 photocatalytic nanomaterials, Int. J. Environ. Sci. Technol. 16 (2019) 4975–4988, doi:10.1007/s13762-019-02385-5.

[35] C.C. Mardare, A.W. Hassel, Review on the versatility of tungsten oxide coatings, Phys. Status Solidi Appl. Mater. Sci. 216 (2019) 1–16, doi:10.1002/pssa.201900047.

[36] C.M. Wu, S. Naseem, M.H. Chou, J.H. Wang, Y.Q. Jian, Recent advances in tungsten-oxide-based materials and their applications, Front. Mater. 6 (2019) 1–17, doi:10.3389/fmats.2019.00049.

[37] Y.M. Hunge, M.A. Mahadik, S.S. Kumbhar, V.S. Mohite, K.Y. Rajpure, N.G. Deshpande, A.V. Moholkar, C.H. Bhosale, Visible light catalysis of methyl orange using nanostructured WO_3 thin films, Ceram. Int. 42 (2016) 789–798, doi:10.1016/j.ceramint.2015.08.178.

[38] Y.P. Xie, G. Liu, L. Yin, H.-.M. Cheng, Crystal facet-dependent photocatalytic oxidation and reduction reactivity of monoclinic WO_3 for solar energy conversion, J. Mater. Chem. 22 (2012) 6746, doi:10.1039/c2jm16178h.

[39] Y. Li, Z. Tang, J. Zhang, Z. Zhang, Exposed facet and crystal phase tuning of hierarchical tungsten oxide nanostructures and their enhanced visible-light-driven photocatalytic performance, CrystEngComm 17 (2015) 9102–9110, doi:10.1039/c5ce01829c.

[40] H. Zhang, J. Yang, D. Li, W. Guo, Q. Qin, L. Zhu, W. Zheng, Template-free facile preparation of monoclinic WO_3 nanoplates and their high photocatalytic activities, Appl. Surf. Sci. 305 (2014) 274–280, doi:10.1016/j.apsusc.2014.03.061.

[41] A. Bayu, D. Nandiyanto, R. Zaen, R. Oktiani, Correlation between crystallite size and photocatalytic performance of micrometer-sized monoclinic WO_3 particles, Arab. J. Chem. 13 (2020) 1283–1296, doi:10.1016/j.arabjc.2017.10.010.

[42] B. Bhuyan, B. Paul, S.S. Dhar, S. Vadivel, Facile hydrothermal synthesis of ultrasmall $W_{18}O_{49}$ nanoparticles and studies of their photocatalytic activity towards degradation of methylene blue, Mater. Chem. Phys. 188 (2017) 1–7, doi:10.1016/j.matchemphys.2016.12.035.

[43] H. Zhao, Q. Fang, C. Chen, Z. Chao, Y. Tsang, Y. Wu, WO_3 quantum dots decorated GO/Mg-doped ZnO composites for enhanced photocatalytic activity under nature sunlight, Appl. Organomet. Chem. 32 (2018) 1–10, doi:10.1002/aoc.4449.

[44] C. Chen, X. Liu, H. Long, F. Ding, Q. Liu, X. Chen, Preparation and photocatalytic performance of graphene oxide/WO_3 quantum Dots/TiO_2@SiO_2 microspheres, Vacuum 164 (2019) 66–71, doi:10.1016/j.vacuum.2019.03.002.

[45] X. Wang, H. Fan, P. Ren, Effects of exposed facets on photocatalytic properties of WO_3, Adv. Powder Technol. 28 (2017) 2549–2555, doi:10.1016/j.apt.2017.07.005.

[46] X. Liu, C. Chen, X. Chen, G. Qian, J. Wang, C. Wang, Z. Cao, Q. Liu, WO_3 QDs enhanced photocatalytic and electrochemical perfomance of GO/TiO_2 composite, Catal. Today 315 (2018) 155–161, doi:10.1016/j.cattod.2018.02.037.

[47] Y.Y. Li, Z. Tang, J. Zhang, Z. Zhang, Enhanced photocatalytic performance of tungsten oxide through tuning exposed facets and introducing oxygen vacancies, J. Alloys Compd. 708 (2017) 358–366, doi:10.1016/j.jallcom.2017.03.046.

[48] N. Zhang, C. Chen, Z. Mei, X. Liu, X. Qu, Y. Li, S. Li, W. Qi, Y. Zhang, J. Ye, V.A.L. Roy, R. Ma, Monoclinic tungsten oxide with {100} facet orientation and tuned electronic band structure for enhanced photocatalytic oxidations, ACS Appl. Mater. Interfaces 8 (2016) 10367–10374, doi:10.1021/acsami.6b02275.

[49] C. Wang, S. Luo, C. Liu, C. Chen, WO_3 quantum dots enhanced the photocatalytic performances of graphene oxide/TiO_2 films under flowing dye solution, Inorg. Chem. Commun. 115 (2020) 107875, doi:10.1016/j.inoche.2020.107875.

[50] Q. Xiao, L. Gao, One-step hydrothermal synthesis of C, W-codoped mesoporous TiO_2 with enhanced visible light photocatalytic activity, J. Alloys Compd. 551 (2013) 286–292, doi:10.1016/j.jallcom.2012.10.040.

[51] F. Wang, C. Di Valentin, G. Pacchioni, Doping of WO_3 for photocatalytic water splitting: hints from density functional theory, J. Phys. Chem. C 116 (2012) 8901–8909, doi:10.1021/jp300867j.

[52] A. Yan, C. Xie, F. Huang, S.S. Zhang, S.S. Zhang, An efficient method to modulate the structure, morphology and properties of WO_3 through niobium doping, J. Alloys Compd. 610 (2014) 132–137, doi:10.1016/j.jallcom.2014.04.188.

[53] F. Huang, A. Yan, H. Zhao, Influences of doping on photocatalytic properties of TiO_2 photocatalyst, in: W. Cao (Ed.), Semiconductor Photocatalysis – Materials, Mechanisms and Applications, 1st ed., IntechOpen, Xuzhou, 2016, p. 51, doi:10.5772/63234.

[54] S.L. Liew, Z. Zhang, T.W.G. Goh, G.S. Subramanian, H.L.D. Seng, T.S.A. Hor, H.K. Luo, D.Z. Chi, Yb-doped WO_3 photocatalysts for water oxidation with visible light, Int. J. Hydrogen Energy 39 (2014) 4291–4298, doi:10.1016/j.ijhydene.2013.12.204.

[55] C. Feng, S. Wang, B. Geng, Ti(iv) doped WO_3 nanocuboids: fabrication and enhanced visible-light-driven photocatalytic performance, Nanoscale 3 (2011) 3695, doi:10.1039/c1nr10460h.

[56] M.A. Gondal, M.A. Suliman, M.A. Dastageer, G.K. Chuah, C. Basheer, D. Yang, A. Suwaiyan, Visible light photocatalytic degradation of herbicide (Atrazine) using surface plasmon resonance induced in mesoporous Ag-WO_3/SBA-15 composite, J. Mol. Catal. A Chem. 425 (2016) 208–216, doi:10.1016/j.molcata.2016.10.015.

[57] L. Wenzhang, L. Jie, W. Xuan, C. Qiyuan, Preparation and water-splitting photocatalytic behavior of S-doped WO_3, Appl. Surf. Sci. 263 (2012) 157–162.

[58] W. Li, F. Zhan, J. Li, C. Liu, Y. Yang, Y. Li, Q. Chen, Enhancing photoelectrochemical water splitting by aluminum-doped plate-like WO_3 electrodes, Electrochim. Acta 160 (2015) 57–63, doi:10.1016/j.electacta.2015.01.095.

[59] S.S. Kalanur, I.H. Yoo, K. Eom, H. Seo, Enhancement of photoelectrochemical water splitting response of WO_3 by means of Bi doping, J. Catal. 357 (2018) 127–137, doi:10.1016/j.jcat.2017.11.012.

[60] H. Song, Y. Li, Z. Lou, M. Xiao, L. Hu, Z. Ye, L. Zhu, Synthesis of Fe-doped WO_3 nanostructures with high visible-light-driven photocatalytic activities, Appl. Catal. B: Environ. 166–167 (2015) 112–120, doi:10.1016/j.apcatb.2014.11.020.

[61] M. Qamar, Z.H. Yamani, M.A. Gondal, K. Alhooshani, Synthesis and comparative photocatalytic activity of Pt/$WO_3$and Au/WO_3 nanocomposites under sunlight-type excitation, Solid State Sci. 13 (2011) 1748–1754, doi:10.1016/j.solidstatesciences.2011.07.002.

[62] Z. Wen, W. Wu, Z. Liu, H. Zhang, J. Li, J. Chen, Ultrahigh-efficiency photocatalysts based on mesoporous Pt–WO_3 nanohybrids, Phys. Chem. Chem. Phys. 15 (2013) 6773, doi:10.1039/c3cp50647a.

[63] M.A. Gondal, A. Bagabas, A. Dastageer, A. Khalil, Synthesis, characterization, and antimicrobial application of nano-palladium-doped nano-WO_3, J. Mol. Catal. A Chem. 323 (2010) 78–83, doi:10.1016/j.molcata.2010.03.019.

[64] P. Dong, N. Xu, Y. Xu, X. Wang, A study of Pt/WO_3-carrier catalysts for photocatalytic purification of NO gas, Catal. Commun. 84 (2016) 142–146, doi:10.1016/j.catcom.2016.06.027.

[65] B. Ma, J. Guo, W.L. Dai, K. Fan, Ag-AgCl/WO_3 hollow sphere with flower-like structure and superior visible photocatalytic activity, Appl. Catal. B: Environ. 123–124 (2012) 193–199, doi:10.1016/j.apcatb.2012.04.029.

[66] J. Ding, L. Zhang, Q. Liu, W.L. Dai, G. Guan, Synergistic effects of electronic structure of WO_3 nanorods with the dominant {001} exposed facets combined with silver size-dependent on the visible-light photocatalytic activity, Appl. Catal. B: Environ. 203 (2017) 335–342, doi:10.1016/j.apcatb.2016.10.028.

[67] R. Adhikari, G. Gyawali, T. Sekino, S.Wohn Lee, Microwave assisted hydrothermal synthesis of Ag/AgCl/WO_3 photocatalyst and its photocatalytic activity under simulated solar light, J. Solid State Chem. 197 (2013) 560–565, doi:10.1016/j.jssc.2012.08.012.

[68] A. Hameed, I.M.I. Ismail, M. Aslam, M.A. Gondal, Photocatalytic conversion of methane into methanol: performance of silver impregnated WO_3, Appl. Catal. A: Gen. 470 (2014) 327–335, doi:10.1016/j.apcata.2013.10.045.

[69] Q. Xiang, G.F. Meng, H.B. Zhao, Y. Zhang, H. Li, W.J. Ma, J.Q. Xu, Au nanoparticle modified WO_3 nanorods with their enhanced properties for photocatalysis and gas sensing, J. Phys. Chem. C 114 (2010) 2049–2055, doi:10.1021/jp909742d.

[70] X. Chang, S. Sun, Y. Zhou, L. Dong, Y. Yin, Solvothermal synthesis of Ce-doped tungsten oxide nanostructures as visible-light-driven photocatalysts, Nanotechnology 22 (2011), doi:10.1088/0957-4484/22/26/265603.

[71] C. Wang, L. Cao, Preparation, spectral characteristics and photocatalytic activity of Eu^{3+}-doped WO_3 nanoparticles, J. Rare Earths 29 (2011) 727–731, doi:10.1016/S1002-0721(10)60531-5.

[72] K. Villa, S. Murcia-López, J.R. Morante, T. Andreu, An insight on the role of La in mesoporous WO_3 for the photocatalytic conversion of methane into methanol, Appl. Catal. B: Environ. 187 (2016) 30–36, doi:10.1016/j.apcatb.2016.01.032.

[73] L. Xu, D. Gu, X. Chang, L. Chai, Z. Li, X. Jin, S. Sun, Rare-earth-doped tungsten oxide microspheres with highly enhanced photocatalytic activites, Ceram. Int. 43 (2017) 10263–10269, doi:10.1016/j.ceramint.2017.05.055.

[74] M.B. Tahir, G. Nabi, N.R. Khalid, M. Rafique, Role of europium on WO_3 performance under visible-light for photocatalytic activity, Ceram. Int. 44 (2018) 5705–5709, doi:10.1016/j.ceramint.2017.12.223.

[75] H. Liu, T. Peng, D. Ke, Z. Peng, C. Yan, Preparation and photocatalytic activity of dysprosium doped tungsten trioxide nanoparticles, Mater. Chem. Phys. 104 (2007) 377–383, doi:10.1016/j.matchemphys.2007.03.028.

[76] Y. Liu, J. Li, W. Li, Y. Yang, Y. Li, Q. Chen, Enhancement of the photoelectrochemical performance of WO_3 vertical arrays film for solar water splitting by gadolinium doping, J. Phys. Chem. C 119 (2015) 14834–14842, doi:10.1021/acs.jpcc.5b00966.

[77] X. Zhu, P. Zhang, B. Li, Q. Hu, W. Su, L. Dong, F. Wang, Preparation, characterization and photocatalytic properties of La/WO_3 composites, J. Mater. Sci. Mater. Electron. 28 (2017) 12158–12167, doi:10.1007/s10854-017-7030-3.

[78] T. Zhang, Z. Zhu, H. Chen, Y. Bai, S. Xiao, X. Zheng, Q. Xue, S. Yang, Iron-doping-enhanced photoelectrochemical water splitting performance of nanostructured WO_3: a combined experimental and theoretical study, Nanoscale 7 (2015) 2933–2940, doi:10.1039/C4NR07024K.

[79] I.A. Mkhalid, Photocatalytic degradation of herbicides under visible light using Pd-WO_3 nanorods, Ceram. Int. 42 (2016) 15975–15980, doi:10.1016/j.ceramint.2016.07.100.

[80] S. Sun, W. Wang, S. Zeng, M. Shang, L. Zhang, Preparation of ordered mesoporous Ag/WO_3 and its highly efficient degradation of acetaldehyde under visible-light irradiation, J. Hazard. Mater. 178 (2010) 427–433, doi:10.1016/j.jhazmat.2010.01.098.

[81] T. Govindaraj, C. Mahendran, R. Marnadu, M. Shkir, V.S. Manikandan, The remarkably enhanced visible-light-photocatalytic activity of hydrothermally synthesized WO_3 nanorods : an effect of Gd doping, Ceram. Int. (2020), doi:10.1016/j.ceramint.2020.10.004.

[82] H. Sudrajat, S. Babel, Role of reactive species in the photocatalytic degradation of amaranth by highly active N-doped WO_3, Bull. Mater. Sci. 40 (2017) 1421–1428, doi:10.1007/s12034-017-1502-1.

[83] F. Han, H. Li, L. Fu, J. Yang, Z. Liu, Synthesis of S-doped WO_3 nanowires with enhanced photocatalytic performance towards dye degradation, Chem. Phys. Lett. 651 (2016) 183–187, doi:10.1016/j.cplett.2016.03.017.

[84] Y.W. Choi, S. Kim, M. Seong, H. Yoo, J. Choi, NH_4-doped anodic WO_3 prepared through anodization and subsequent NH_4OH treatment for water splitting, Appl. Surf. Sci. 324 (2015) 414–418, doi:10.1016/j.apsusc.2014.10.059.

[85] Q. Mi, Y. Ping, Y. Li, B. Cao, B.S. Brunschwig, P.G. Khalifah, G.A. Galli, H.B. Gray, N.S. Lewis, Thermally stable N_2-Intercalated WO_3 photoanodes for water oxidation, J. Am. Chem. Soc. 134 (2012) 18318–18324, doi:10.1021/ja3067622.

[86] H. Sudrajat, S. Babel, Rapid photocatalytic degradation of the recalcitrant dye amaranth by highly active N-WO_3, Environ. Chem. Lett. 14 (2016) 243–249, doi:10.1007/s10311-015-0538-y.

[87] Y.C. Nah, I. Paramasivam, R. Hahn, N.K. Shrestha, P. Schmuki, Nitrogen doping of nanoporous WO_3 layers by NH_3 treatment for increased visible light photoresponse, Nanotechnology 21 (2010), doi:10.1088/0957-4484/21/10/105704.

[88] A.J.E. Rettie, K.C. Klavetter, J.F. Lin, A. Dolocan, H. Celio, A. Ishiekwene, H.L. Bolton, K.N. Pearson, N.T. Hahn, C.B. Mullins, Improved visible light harvesting of WO_3 by incorporation of sulfur or iodine: a tale of two impurities, Chem. Mater. 26 (2014) 1670–1677, doi:10.1021/cm403969r.

[89] Y. Sun, C.J. Murphy, K.R. Reyes-Gil, E.A. Reyes-Garcia, J.M. Thornton, N.A. Morris, D. Raftery, Photoelectrochemical and structural characterization of carbon-doped WO_3 films prepared via spray pyrolysis, Int. J. Hydrogen Energy 34 (2009) 8476–8484, doi:10.1016/j.ijhydene.2009.08.015.

[90] Y. Zheng, G. Chen, Y. Yu, Y. Zhou, F. He, Synthesis of carbon doped $WO_3 \bullet 0 \bullet 33H_2O$ hierarchical photocatalyst with improved photocatalytic activity, Appl. Surf. Sci. 362 (2016) 182–190, doi:10.1016/j.apsusc.2015.11.115.

[91] Y. Yang, G. Jin, H. Li, Photoelectrochemical properties and photocatalytic activity of fluorine-doped plate-like WO_3 from hydrothermal radio-frequency (RF) sputtered tungsten thin films, Nano 12 (2017) 17–21, doi:10.1142/S1793292017500412.

[92] G.H. Jin, S.Q. Liu, Preparation and photocatalytic activity of fluorine doped WO_3 under uv and visible light, Dig. J. Nanomater. Biostruct. 11 (2016) 1179–1188.

[93] J.O. Tijani, O. Ugochukwu, L.A. Fadipe, M.T. Bankole, A.S. Abdulkareem, W.D. Roos, Photocatalytic degradation of local dyeing wastewater by iodine-phosphorus co-doped tungsten trioxide nanocomposites under natural sunlight irradiation, J. Environ. Manag. 236 (2019) 519–533, doi:10.1016/j.jenvman.2019.02.027.

[94] Y. Zheng, G. Chen, Y. Yu, Y. Zhou, F. He, Synthesis of carbon doped $WO_3 \bullet 0 \bullet 33H_2O$ hierarchical photocatalyst with improved photocatalytic activity, Appl. Surf. Sci. 362 (2016) 182–190, doi:10.1016/j.apsusc.2015.11.115.

[95] A. Meng, B. Zhu, B. Zhong, L. Zhang, B. Cheng, Direct Z-scheme TiO_2/CdS hierarchical photocatalyst for enhanced photocatalytic H_2-production activity, Appl. Surf. Sci. 422 (2017) 518–527, doi:10.1016/j.apsusc.2017.06.028.

[96] Y. Miseki, S. Fujiyoshi, T. Gunji, K. Sayama, Photocatalytic water splitting under

visible light utilizing I^{3-}/I^- and IO^{3-}/I^- redox mediators by Z-scheme system using surface treated PtO_x/WO_3 as O_2 evolution photocatalyst, Catal. Sci. Technol. 3 (2013) 1750–1756, doi:10.1039/c3cy00055a.

[97] A. Khampuanbut, S. Santalelat, A. Pankiew, D. Channei, S. Pornsuwan, K. Faungnawakij, S. Phanichphant, B. Inceesungvorn, Visible-light-driven WO_3/BiOBr heterojunction photocatalysts for oxidative coupling of amines to imines: energy band alignment and mechanistic insight, J. Colloid Interface Sci. 560 (2020) 213–224, doi:10.1016/j.jcis.2019.10.057.

[98] R. Wang, G. Qiu, Y. Xiao, X. Tao, W. Peng, B. Li, Optimal construction of $WO_3 \bullet H_2O$/Pd/CdS ternary Z-scheme photocatalyst with remarkably enhanced performance for oxidative coupling of benzylamines, J. Catal. 374 (2019) 378–390, doi:10.1016/j.jcat.2019.05.016.

[99] L. Jiang, X. Yuan, G. Zeng, J. Liang, X. Chen, H. Yu, H. Wang, Z. Wu, J. Zhang, T. Xiong, In-situ synthesis of direct solid-state dual Z-scheme WO_3/g-C_3N_4/Bi_2O_3 photocatalyst for the degradation of refractory pollutant, Appl. Catal. B: Environ. 227 (2018) 376–385, doi:10.1016/j.apcatb.2018.01.042.

[100] H. Du, Y.N. Liu, C.C. Shen, A.W. Xu, Nanoheterostructured photocatalysts for improving photocatalytic hydrogen production, Cuihua Xuebao/Chin. J. Catal. 38 (2017) 1295–1306, doi:10.1016/S1872-2067(17)62866-3.

[101] M.A. Gondal, M.A. Dastageer, L.E. Oloore, U. Baig, Laser induced selective photo-catalytic reduction of CO_2 into methanol using In_2O_3-WO_3 nano-composite, J. Photochem. Photobiol. A Chem. 343 (2017) 40–50, doi:10.1016/j.jphotochem.2017.04.016.

[102] C. Sotelo-Vazquez, R. Quesada-Cabrera, M. Ling, D.O. Scanlon, A. Kafizas, P.K. Thakur, T.L. Lee, A. Taylor, G.W. Watson, R.G. Palgrave, J.R. Durrant, C.S. Blackman, I.P. Parkin, Evidence and effect of photogenerated charge transfer for enhanced photocatalysis in WO_3/TiO_2 heterojunction films: a computational and experimental study, Adv. Funct. Mater. 27 (2017) 1–10, doi:10.1002/adfm.201605413.

[103] N.A. Ramos-Delgado, M.A. Gracia-Pinilla, L. Maya-Treviño, L. Hinojosa-Reyes, J.L. Guzman-Mar, A. Hernández-Ramírez, Solar photocatalytic activity of TiO_2 modified with WO_3 on the degradation of an organophosphorus pesticide, J. Hazard. Mater. 263 (2013) 36–44, doi:10.1016/j.jhazmat.2013.07.058.

[104] I.A. Castro, G. Byzynski, M. Dawson, C. Ribeiro, Charge transfer mechanism of WO_3/TiO_2 heterostructure for photoelectrochemical water splitting, J. Photochem. Photobiol. A: Chem. 339 (2017) 95–102, doi:10.1016/j.jphotochem.2017.02.024.

[105] E. Muguntha, M.B. Saidutta, P.E. Jagadeeshbabu, Photocatalytic activity of ZnO-WO_3 for diclofenac degradation under visible light irradiation, J. Photochem. Photobiol. A: Chem. 383 (2019) 111993, doi:10.1016/j.jphotochem.2019.111993.

[106] S.M. Lam, J.C. Sin, A.Z. Abdullah, A.R. Mohamed, Sunlight responsive WO_3/ZnO nanorods for photocatalytic degradation and mineralization of chlorinated phenoxyacetic acid herbicides in water, J. Colloid Interface Sci. 450 (2015) 34–44, doi:10.1016/j.jcis.2015.02.075.

[107] J. Zheng, F. Chang, M. Jiao, Q. Xu, B. Deng, X. Hu, A visible-light-driven heterojuncted composite $WO_3/Bi_{12}O_{17}Cl_2$: synthesis, characterization, and improved photocatalytic performance, J. Colloid Interface Sci. 510 (2018) 20–31, doi:10.1016/j.jcis.2017.07.119.

[108] B.S. Kalanoor, H. Seo, S.S. Kalanur, Recent developments in photoelectrochemical water-splitting using $WO_3/BiVO_4$ heterojunction photoanode: a review, Mater. Sci. Energy Technol. 1 (2018) 49–62, doi:10.1016/j.mset.2018.03.004.

[109] W. Sun, S. Cui, N. Wei, S. Chen, Y. Liu, D. Wang, Hierarchical WO_3/TiO_2 nanotube nanocomposites for efficient photocathodic protection of 304 stainless steel under visible light, J. Alloys Compd. 749 (2018) 741–749, doi:10.1016/j.jallcom.2018.03.371.

[110] Z. Zhou, Z. Wu, Q. Xu, G. Zhao, A solar-charged photoelectrochemical wastewater fuel cell for efficient and sustainable hydrogen production, J. Mater. Chem. A 5 (2017) 25450–25459, doi:10.1039/c7ta08112j.

[111] Y. Li, L. Zhang, R. Liu, Z. Cao, X. Sun, X. Liu, J. Luo, WO_3@α-Fe_2O_3 heterojunction arrays with improved photoelectrochemical behavior for neutral pH water splitting, ChemCatChem 8 (2016) 2765–2770, doi:10.1002/cctc.201600475.

[112] P. Wu, Z. Liu, D. Chen, M. Zhou, J. Wei, Flake-like NiO/WO_3 p-n heterojunction photocathode for photoelectrochemical water splitting, Appl. Surf. Sci. 440 (2018) 1101–1106, doi:10.1016/j.apsusc.2018.01.292.

[113] J. Zhang, H. Ma, Z. Liu, Highly efficient photocatalyst based on all oxides WO_3/Cu_2O heterojunction for photoelectrochemical water splitting, Appl. Catal. B: Environ. 201 (2017) 84–91, doi:10.1016/j.apcatb.2016.08.025.

[114] J. Huang, Y. Zhang, Y. Ding, Rationally designed/constructed CoO_x/WO_3 anode for efficient photoelectrochemical water oxidation, ACS Catal. 7 (2017) 1841–1845, doi:10.1021/acscatal.7b00022.

[115] M.G. Lee, D.H. Kim, W. Sohn, C.W. Moon, H. Park, S. Lee, H.W. Jang, Conformally coated $BiVO_4$ nanodots on porosity-controlled WO_3 nanorods as highly efficient type II heterojunction photoanodes for water oxidation, Nano Energy 28 (2016) 250–260, doi:10.1016/j.nanoen.2016.08.046.

[116] Y. Wang, W. Tian, L. Chen, F. Cao, J. Guo, L. Li, Three-dimensional WO_3 nanoplate/Bi_2S_3 Nanorod heterojunction as a highly efficient photoanode for improved photoelectrochemical water splitting, ACS Appl. Mater. Interfaces 9 (2017) 40235–40243, doi:10.1021/acsami.7b11510.

[117] Y. Wang, C. Chen, W. Tian, W. Xu, L. Li, Designing $WO_3/CdIn_2S_4$ type-II heterojunction with both efficient light absorption and charge separation for enhanced photoelectrochemical water splitting, Nanotechnology 30 (2019) 10.

[118] S.Y. Chae, C.S. Lee, H. Jung, O.S. Joo, B.K. Min, J.H. Kim, Y.J. Hwang, Insight into charge separation in $WO_3/BiVO_4$ heterojunction for solar water splitting, ACS Appl. Mater. Interfaces 9 (2017) 19780–19790, doi:10.1021/acsami.7b02486.

[119] S.M. Lam, J.C. Sin, H. Lin, H. Li, J.W. Lim, H. Zeng, A Z-scheme WO_3 loaded-hexagonal rod-like ZnO/Zn photocatalytic fuel cell for chemical energy recuperation from food wastewater treatment, Appl. Surf. Sci. 514 (2020) 145945, doi:10.1016/j.apsusc.2020.145945.

[120] Q. Zeng, J. Bai, J. Li, L. Li, L. Xia, B. Zhou, Y. Sun, Highly-stable and efficient photocatalytic fuel cell based on an epitaxial TiO_2/WO_3/W nanothorn photoanode and enhanced radical reactions for simultaneous electricity production and wastewater treatment, Appl. Energy 220 (2018) 127–137, doi:10.1016/j.apenergy.2018.03.042.

[121] M. Li, Y. Liu, L. Dong, C. Shen, F. Li, M. Huang, C. Ma, B. Yang, X. An, W. Sand, Recent advances on photocatalytic fuel cell for environmental applications—the marriage of photocatalysis and fuel cells, Sci. Total Environ. 668 (2019) 966–978, doi:10.1016/j.scitotenv.2019.03.071.

[122] T. Xu, Y. Wang, X. Zhou, X. Zheng, Q. Xu, Z. Chen, Y. Ren, B. Yan, Fabrication and assembly of two-dimensional $TiO_2/WO_3 \bullet H_2O$ heterostructures with type II band alignment for enhanced photocatalytic performance, Appl. Surf. Sci. 403 (2017) 564–571, doi:10.1016/j.apsusc.2017.01.242.

[123] X. Yuan, L. Jiang, X. Chen, L. Leng, H. Wang, Z. Wu, T. Xiong, G. Zeng, Highly efficient visible-light-induced photoactivity of Z-scheme $Ag_2CO_3/Ag/WO_3$ photocatalyst for organic pollutant degradation, Environ. Sci. Nano 4 (2017) 2175–2185, doi:10.1039/c7en00713b.

[124] X. Zhang, R. Zhang, S. Niu, J. Zheng, C. Guo, Construction of core-shell structured WO_3@SnS_2 hetero-junction as a direct Z-scheme photo-catalyst, J. Colloid Interface Sci. 554 (2019) 229–238, doi:10.1016/j.jcis.2019.06.107.

[125] S.B. Rawal, H.J. Kang, D. Won, W.I. Lee, Novel $ZnFe_2O_4/WO_3$ a highly efficient visible-light photocatalytic system operated by a Z-scheme mechanism, Appl. Catal. B: Environ. 256 (2019) 117856, doi:10.1016/j.apcatb.2019.117856.

[126] A.J. Bard, Photoelectrochemistry and heterogeneous photocatalysis at semiconductors, J. Photochem. 10 (1979) 59–75.

[127] Q. Li, F. Wang, Y. Hua, Y. Luo, X. Liu, G. Duan, X. Yang, Deposition-precipitation preparation of $Ag/Ag_3PO_4/WO_3$ nanocomposites for efficient Visible-light degradation of rhodamine B under strongly acidic / alkaline conditions, J. Colloid Interface Sci. 506 (2017) 207–216, doi:10.1016/j.jcis.2017.07.018.

[128] C. Shifu, J. Lei, T. Wenming, F. Xianliang, Fabrication, characterization and mechanism of a novel Z-scheme photocatalyst $NaNbO_3/WO_3$ with enhanced photocatalytic activity, Dalton Trans. 42 (2013) 10759–10768, doi:10.1039/c3dt50699a.

[129] K. Sayama, K. Mukasa, R. Abe, Y. Abe, H. Arakawa, Stoichiometric water splitting into H_2 and O_2 using a mixture of two different photocatalysts and an IO_3^-/I_- shuttle redox mediator under visible light irradiation, Chem. Commun. 1 (2001) 2416–2417, doi:10.1039/b107673f.

[130] L. Ye, Z. Wen, $ZnIn_2S_4$ nanosheets decorating WO_3 nanorods core-shell hybrids for boosting visible-light photocatalysis hydrogen generation, Int. J. Hydrogen Energy 44 (2019) 3751–3759, doi:10.1016/j.ijhydene.2018.12.093.

[131] J. Zhang, J. Liu, X. Wang, J. Mai, W. Zhao, Z. Ding, Y. Fang, Construction of Z-scheme tungsten trioxide nanosheets-nitrogen-doped carbon dots composites for the enhanced photothermal synergistic catalytic oxidation of cyclohexane, Appl. Catal. B: Environ. 259 (2019) 118063, doi:10.1016/j.apcatb.2019.118063.

[132] D. Liu, Y. Xu, M. Sun, Y. Huang, Y. Yu, B. Zhang, Photothermally assisted photocatalytic conversion of CO_2-H_2O into fuels over a WN-WO_3 Z-scheme heterostructure, J. Mater. Chem. A 8 (2020) 1077–1083, doi:10.1039/c9ta10629d.

[133] S.H. Chen, J.H. Su, H. yu Lin, New Modified sol–gel method for the preparation KNb_3O_8 as a hydrogen evolution photocatalyst in Z-scheme overall water splitting, Top. Catal. (2020) 1–9, doi:10.1007/s11244-020-01272-5.

[134] H. Tada, T. Mitsui, T. Kiyonaga, T. Akita, K. Tanaka, All-solid-state Z-scheme in CdS-Au-TiO_2 three-component nanojunction system, Nat. Mater. 5 (2006) 782–786, doi:10.1038/nmat1734.

[135] Y.Wen Teh, Y.Wei Goh, X.Ying Kong, B.J. Ng, S.T. Yong, S.P. Chai, Fabrication of $Bi_2WO_6/Cu/WO_3$ all-solid-state Z-scheme composite photocatalyst to improve CO_2 photoreduction under visible light irradiation, ChemCatChem 11 (2019) 6431–6438, doi:10.1002/cctc.201901653.

[136] H. Li, H. Yu, X. Quan, S. Chen, Y. Zhang, Uncovering the key role of the fermi level of the electron mediator in a Z-Scheme photocatalyst by detecting the charge transfer process of WO_3-metal-gC_3N_4 (Metal = Cu, Ag, Au), ACS Appl. Mater. Interfaces 8 (2016) 2111–2119, doi:10.1021/acsami.5b10613.

[137] Q. Li, J. Yao, M. Arif, T. Huang, X. Liu, G. Duan, Facile fabrication and photocatalytic performance of WO_3 nanoplates in situ decorated with Ag/β-Ag_2WO_4 nanoparticles, J. Environ. Chem. Eng. 6 (2018) 1969–1978, doi:10.1016/j.jece.2018.02.034.

[138] X. Zeng, Z. Wang, G. Wang, T.R. Gengenbach, D.T. Mccarthy, A. Deletic, J. Yu, X. Zhang, Highly dispersed TiO_2 nanocrystals and WO_3 nanorods on reduced graphene oxide : z-scheme photocatalysis system for accelerated photocatalytic water disinfection, Appl. Catal. B: Environ. 218 (2017) 163–173, doi:10.1016/j.apcatb.2017.06.055.

[139] G. Li, J. Hou, W. Zhang, P. Li, G. Liu, Y. Wang, K. Wang, Graphene-bridged WO_3/MoS_2 Z-scheme photocatalyst for enhanced photodegradation under visible light irradiation, Mater. Chem. Phys. 246 (2020) 122827, doi:10.1016/j.matchemphys.2020.122827.

[140] T. Wang, W. Quan, D. Jiang, L. Chen, D. Li, S. Meng, M. Chen, Synthesis of redox-mediator-free direct Z-scheme AgI/WO_3 nanocomposite photocatalysts for the degradation of tetracycline with enhanced photocatalytic activity, Chem. Eng. J. 300 (2016) 280–290, doi:10.1016/j.cej.2016.04.128.

[141] X. Liu, A. Jin, Y. Jia, T. Xia, C. Deng, M. Zhu, C. Chen, X. Chen, Synergy of adsorption and visible-light photocatalytic degradation of methylene blue by a bifunctional Z-scheme heterojunction of WO_3/g-C_3N_4, Appl. Surf. Sci. 405 (2017) 359–371, doi:10.1016/J.APSUSC.2017.02.025.

[142] J. Zhang, Y. Ma, Y. Du, H. Jiang, D. Zhou, S. Dong, Carbon nanodots/WO_3 nanorods Z-scheme composites : remarkably enhanced photocatalytic perfor-

mance under broad spectrum, Appl. Catal. B: Environ. 209 (2017) 253–264, doi:10.1016/j.apcatb.2017.03.017.

[143] C.T.K. Nguyen, N. Quang Tran, S. Seo, H. Hwang, S. Oh, J. Yu, J. Lee, T. Anh Le, J. Hwang, M. Kim, H. Lee, Highly efficient nanostructured metal-decorated hybrid semiconductors for solar conversion of CO_2 with almost complete CO selectivity, Mater. Today 35 (2020) 25–33, doi:10.1016/j.mattod.2019.11.005.

[144] W. Shi, X. Guo, C. Cui, K. Jiang, Z. Li, L. Qu, J.C. Wang, Controllable synthesis of Cu_2O decorated WO_3 nanosheets with dominant (0 0 1) facets for photocatalytic CO_2 reduction under visible-light irradiation, Appl. Catal. B: Environ. 243 (2019) 236–242, doi:10.1016/j.apcatb.2018.09.076.

[145] W. Shi, X. Guo, J.C. Wang, Y. Li, L. Liu, Y. Hou, Y. Li, H. Lou, Enhanced photocatalytic 3D/2D architecture for CO_2 reduction over cuprous oxide octahedrons supported on hexagonal phase tungsten oxide nanoflakes, J. Alloys Compd. 830 (2020) 2–8, doi:10.1016/j.jallcom.2020.154683.

[146] J. Jin, J. Yu, D. Guo, C. Cui, W. Ho, A hierarchical Z-scheme CdS-WO_3 photocatalyst with enhanced CO_2 reduction activity, Small 11 (2015) 5262–5271, doi:10.1002/smll.201500926.

[147] J. Wang, Y. Zhang, X. Wang, W. Su, Simultaneous enhancements in photoactivity and anti-photocorrosion of Z-scheme $Mn_{0.25}Cd_{0.75}S/WO_3$ for solar water splitting, Appl. Catal. B: Environ. 268 (2020) 118444, doi:10.1016/j.apcatb.2019.118444.

[148] G. Yang, D. Chen, H. Ding, J. Feng, J.Z. Zhang, Y. Zhu, S. Hamid, D.W. Bahnemann, Well-designed 3D $ZnIn_2S_4$ nanosheets/TiO_2 nanobelts as direct Z-scheme photocatalysts for CO_2 photoreduction into renewable hydrocarbon fuel with high efficiency, Appl. Catal. B: Environ. 219 (2017) 611–618, doi:10.1016/j.apcatb.2017.08.016.

[149] L.J. Zhang, S. Li, B.K. Liu, D.J. Wang, T.F. Xie, Highly efficient CdS/WO_3 photocatalysts: z-scheme photocatalytic mechanism for their enhanced photocatalytic H_2 evolution under visible light, ACS Catal. 4 (2014) 3724–3729, doi:10.1021/cs500794j.

[150] S. Wang, B. Zhu, M. Liu, L. Zhang, J. Yu, M. Zhou, Direct Z-scheme ZnO/CdS hierarchical photocatalyst for enhanced photocatalytic H_2-production activity, Appl. Catal. B: Environ. 243 (2019) 19–26, doi:10.1016/j.apcatb.2018.10.019.

[151] T. Di, B. Zhu, B. Cheng, J. Yu, J. Xu, A direct Z-scheme g-C_3N_4/SnS_2 photocatalyst with superior visible-light CO_2 reduction performance, J. Catal. 352 (2017) 532–541, doi:10.1016/j.jcat.2017.06.006.

[152] L. Ju, Y. Dai, W. Wei, M. Li, B. Huang, DFT investigation on two-dimensional GeS/WS_2 van der Waals heterostructure for direct Z-scheme photocatalytic overall water splitting, Appl. Surf. Sci. 434 (2018) 365–374, doi:10.1016/j.apsusc.2017.10.172.

[153] T. Hu, P. Li, J. Zhang, C. Liang, K. Dai, Highly efficient direct Z-scheme WO_3/CdS-diethylenetriamine photocatalyst and its enhanced photocatalytic H_2 evolution under visible light irradiation, Appl. Surf. Sci. 442 (2018) 20–29, doi:10.1016/j.apsusc.2018.02.146.

[154] M. Tang, Y. Ao, C. Wang, P. Wang, Rationally constructing of a novel dual Z-scheme composite photocatalyst with significantly enhanced performance for neonicotinoid degradation under visible light irradiation, Appl. Catal. B: Environ. 270 (2020) 118918, doi:10.1016/j.apcatb.2020.118918.

[155] J. Feng, T. Jiang, Y. Han, O.K. Okoth, L. Cheng, J. Zhang, Construction of dual Z-scheme Bi_2S_3/Bi_2O_3/WO_3 ternary film with enhanced visible light photoelectrocatalytic performance, Appl. Surf. Sci. 505 (2020) 144632, doi:10.1016/j.apsusc.2019.144632.

[156] H. Zhou, Z. Wen, J. Liu, J. Ke, X. Duan, S. Wang, P. Ag, Z-scheme plasmonic Ag decorated WO_3/Bi_2WO_6 hybrids for enhanced photocatalytic abatement of chlorinated-VOC_s under solar light irradiation, Appl. Catal. B: Environ. 242 (2019) 76–84, doi:10.1016/j.apcatb.2018.09.090.

[157] S. Ali, M. Humayun, W. Pi, Y. Yuan, M. Wang, A. Khan, P. Yue, L. Shu, Z. Zheng, Q. Fu, W. Luo, Fabrication of $BiFeO_3$-g-C_3N_4-WO_3 Z-scheme heterojunction as highly efficient visible-light photocatalyst for water reduction and 2,4-dichlorphenol degradation: insight mechanism, J. Hazard. Mater. 397 (2020), doi:10.1016/j.jhazmat.2020.122708.

[158] F. He, A. Meng, B. Cheng, W. Ho, J. Yu, Enhanced photocatalytic H_2-production activity of WO_3/TiO_2 step-scheme heterojunction by graphene modification, Chin. J. Catal. 41 (2020) 9–20, doi:10.1016/S1872-2067(19)63382-6.

[159] H. Gong, Y. Zhang, Y. Cao, M. Luo, Z. Feng, W. Yang, Pt@Cu_2O/WO_3 composite photocatalyst for enhanced photocatalytic water oxidation performance, Appl. Catal. B: Environ. 237 (2018) 309–317, doi:10.1016/j.apcatb.2018.05.086.

[160] B. Tahir, M. Tahir, M.G. Mohd Nawawi, Well-designed 3D/2D/2D WO_3/Bt/g-C_3N_4 Z-scheme heterojunction for tailoring photocatalytic CO_2 methanation with 2D-layered bentonite-clay as the electron moderator under visible light, Energy Fuels (2020), doi:10.1021/acs.energyfuels.0c02637.

[161] Y. Huang, Z. Guo, H. Liu, S. Zhang, P. Wang, J. Lu, Y. Tong, Heterojunction architecture of N-doped WO_3 nanobundles with Ce_2S_3 nanodots hybridized on a carbon textile enables a highly efficient flexible photocatalyst, Adv. Funct. Mater. 29 (2019) 1–9, doi:10.1002/adfm.201903490.

[162] X. Ma, G. Wang, C. Wang, S. Li, J. Wang, Y. Song, NiS_2 as trapezoid conductive channel modified ternary Z-scheme photocatalyst system,$NiGa_2O_4$/NiS_2/WO_3,for highly photocatalytic simultaneous conversions of NO_2^- and SO_3^{2-}, Chem. Eng. J. 350 (2018) 364–377, doi:10.1016/j.cej.2018.05.149.

[163] A. Raza, H. Shen, A.A. Haidry, L. Sun, R. Liu, S. Cui, Studies of Z-scheme WO_3-TiO_2/Cu_2ZnSnS_4 ternary nanocomposite with enhanced CO_2 photoreduction under visible light irradiation, J. CO_2 Util. 37 (2020) 260–271, doi:10.1016/j.jcou.2019.12.020.